Cenozoic Antarctic Peninsula temperatures and glacial erosion signals from a multi-proxy biomarker study

Emily J. Tibbett[1], Sophie Warny[2], Jessica E. Tierney[3], Julia S. Wellner[4], Sarah J. Feakins[1]

[1]Department of Earth Science, University of Southern California, Los Angeles, CA, USA

[2]Department of Geology and Geophysics, and Museum of Natural Science, Louisiana State University, Baton Rouge, LA, USA

[3]Department of Geosciences, University of Arizona, Tucson, AZ, USA

[4]Department of Earth and Atmospheric Sciences, University of Houston, Houston, TX, USA

Correspondence to: E. J. Tibbett tibbett@usc.edu

Key Points

- Marine sediments provide snapshots of Cenozoic climate conditions on the Antarctic Peninsula
- Terrestrial biomarkers indicate increased reworking of old carbon as cooling and glaciation proceeded
- Soil biomarkers reveal that from the Oligocene to Pliocene, austral summer air temperatures cooled by 7°C, while oceans cooled by 10°C

Abstract

Terrestrial climate records for Antarctica, beyond the age limit of ice cores, are restricted to the few unglaciated areas with exposed rock outcrops. Marine sediments on Antarctica's continental shelves contain records of past oceanic and terrestrial environments that can provide important insights into Antarctic climate evolution. The SHALDRIL II (Shallow Drilling on the Antarctic Continental Margin) expedition recovered sedimentary sequences from the eastern side of the

Antarctic Peninsula that of late Eocene, Oligocene, middle Miocene, and early Pliocene age that provides insights into Cenozoic Antarctic climate and ice sheet development. Here we use biomarker data to assess atmospheric and oceanic temperatures and glacial reworking from the late Eocene to the early Pliocene. Analyses of hopanes and *n*-alkanes that indicate increased erosion of mature (thermally-altered) soil biomarker components reworked by glacial erosion. Branched glycerol dialkyl glycerol tetraethers (GDGTs) from soil bacteria suggest similar air temperatures of 12±1°C (1σ, n = 46) for months above freezing for Eocene, Oligocene, and Miocene timeslices but much colder (and likely shorter) periods of thaw during the Pliocene (5±1°C, n=4) on the Antarctic Peninsula. TEX_{86}-based (Tetraether index of 86 carbons) sea surface temperature (SST) estimates indicate ocean cooling from 7±3°C (n=10) in the Miocene to 3±1°C (n=3) in the Pliocene, consistent with deep ocean cooling. Resulting temperature records provide useful constraints for ice sheet and climate model simulations seeking to improve understanding of ice sheet response under a range of climate conditions.

Plain Language Summary

Records of past climate and ice sheet evolution are preserved in sediment deposited on Antarctica's continental shelves. Using marine sediments allow glimpses of those past conditions in Antarctica. We bring new approaches to revisit the evidence in those sediments. Reworked pollen and soil components show increasing glacial erosion of degraded sediments from land. Soil bacteria grow when soils thaw recording warm season temperatures of 11-12°C in the older sections, but much colder (and likely shorter) summers when there is ice cover. Ocean temperatures cool from 11.5°C to 2.8°C from the oldest section (36 million years ago) to the youngest section (roughly 5 million years ago).

1. Introduction

The Cenozoic is divided into the Greenhouse and Icehouse world with the transition noted by the permanent expansion of high latitude ice sheets (Westerhold et al., 2020). The oxygen isotope increase observed in deep sea sediment (34.2-33.5 Ma) spanning the Eocene-Oligocene boundary (35.9 Ma) reflects the expansion of ice sheets on Antarctica (Carter et al., 2017; Coxall et al., 2005; Coxall & Pearson, 2007). Evidence for glacial expansion across the Antarctic continent is contained in proximal sedimentary deposits around the margins of the continent

(e.g., Passchier et al., 2017; Levy et al., 2019, McKay et al., 2022). In addition, the location of the ice has been reconstructed from evidence that sea level rose around the edges of the continent due to glacial isostatic adjustment, despite the global drop in eustatic sea level (Stocchi et al., 2013). The Antarctic Peninsula may have been among the last areas of the continent to be fully glaciated, given its lower latitude, providing refugia for vegetation (Anderson et al., 2011). However, temperatures remain less well known because previous ice advances scoured the continent and sedimentary archives around the margins are hard to access (McKay et al., 2022). There have been few applications of direct temperature proxies, for example clumped isotopes were applied to the carbonates of shallow-water coastal bivalves of late Eocene age now uplifted on Seymour Island outcrops, east of the Antarctic Peninsula yielding shallow coastal ocean estimates of 11-17°C (Douglas et al., 2014). In the same study, land temperatures determined with soil bacterial branched GDGTs (*br*GDGTs) biomarkers, using the Methylation of Branched Tetraethers (MBT) index estimated a temperature of 13°C (Douglas et al., 2014). During the Oligocene to Miocene, although there was a significant ice sheet, the ocean archaeal biomarker temperature proxy, TEX_{86}, derived from isoprenoidal GDGTs (*iso*GDGTs), at DSDP Site 269 reveals warm ocean temperatures (up to 14°C) persisted off Wilkes Land, East Antarctica (Evangelinos et al., 2020). Soil biomarker *br*GDGTs, and marine biomarker, *iso*GDGTs, were recently applied together to reconstruct land and sea temperatures in marginal sediments for the Eocene Oligocene Transition (EOT) off East Antarctica, in Prydz Bay (Tibbett et al., 2021).

The Antarctic Peninsula is a unique region to study shifts in climate given its location at the far northernmost latitudes of the Antarctic continent, and one of the last areas to be glaciated (Anderson et al., 2011), likely retaining soils and vegetation longer than the more polar areas of the continent and providing an archive of cryosphere-proximal conditions. Due to glacial erosion and uplift of overlying sediments, older sediments are accessible within tens of meters of the seafloor (Anderson & Wellner, 2012). However, the presence of thick multi-year sea ice and iceberg hazards limits drilling operations proximal to the coast. To collect sediment from the Joinville Plateau adjacent to the tip of the Antarctic Peninsula, a drilling rig was added to the RV/IB *Nathaniel B. Palmer* for the SHALDRIL II expedition (Anderson and Wellner, 2012). The sediment collected by SHALDRIL II allows a comparison of climate conditions on the Antarctic Peninsula across the transition from ephemeral ice sheets and alpine glaciers in the Late Eocene to a grounded Antarctic Ice Sheet extending onto the continental shelf by the

Pliocene (Anderson et al., 2011; Bohaty et al., 2011). Pollen analyses indicated a decrease in the diversity of angiosperm-dominated vegetation on the Northern Peninsula as glaciation proceeded (Anderson et al., 2011; Warny & Askin, 2011a,b). Eocene-age sediments in SHALDRIL II Hole 3C yield diverse pollen with decreasing diversity and abundance up-core thought to capture the initial cooling in the latest Eocene (Anderson et al., 2011). In the same samples, the $\delta^{13}C$ of pollen grains revealed increased water stress (Griener et al., 2013) and a 30‰ increase in the δD values of leaf wax which indicates increasing aridity on the Antarctic Peninsula (Feakins et al., 2014). Pollen abundances continued to decline, diversity decreased, and reworking increased in younger sections (Oligocene, Miocene and Pliocene), but absolute temperature estimates are lacking.

Here we revisit SHALDRIL II legacy cores, applying multiple biomarker approaches to reconstruct temperature, vegetation, and erosional context for the Antarctic Peninsula. In particular, we use *n*-alkanes and hopane approaches to assess terrestrial erosion and maturity signals. The *n*-alkanes have long been studied for signals of maturity (e.g., Kvenvolden et al., 1991). The hopane techniques were introduced more recently by Inglis et al. (2018), and recently applied to Antarctic margin sediments in the Ross Sea of Miocene age (Duncan et al., 2019), Prydz Bay sediments across the EOT (Tibbett et al., 2021), and early Eocene sediments off Wilkes Lands (Inglis et al., 2022). Mature biomarkers indicate thermal alteration, and, when identified in the presence of fresh inputs, they identify glacial reworking of the mature components. We generate soil temperatures using the MBT'_{5Me} proxy (Hopmans et al., 2016), and investigate sea surface temperatures using TEX_{86} (Schouten et al., 2007), similar to recent applications to EOT sediments in Prydz Bay (Tibbett et al., 2021). Here we report a multi-biomarker study of SHALDRIL II Holes 3C, 5D and 12A including Eocene, Oligocene, Miocene and Pliocene sediments to capture long term erosion and temperature change. This new record for the Antarctic Peninsula is compared to the demise of vegetation based on pollen concentration from the same sites (Anderson et al., 2011), a compilation of published regional (Antarctic and Southern Ocean) records of temperatures and global signals of atmospheric carbon dioxide, deep ocean temperatures, and ice volume that describe the global Cenozoic cooling trend.

2. Study Sites

The SHALDRIL II expedition was implemented on cruise NBP0602A to the Weddell Sea (Anderson & Wellner, 2012). Hole 3C, cored in the James Ross Basin, (63ºS, 54º39.21'W, and 340 m water depth) and Hole 5D and 12A, from the Joinville Plateau, (corresponding to 63ºS, 52º21.94'W, and 506 m water depth and 63ºS, 52º49.50'W, and 442 m water depth respectively) were used in this study (**Figure 1**).

Prior work has provided age constraints for these sediments based on diatom biostratigraphy with nannofossil and dinoflagellate cyst biostratigraphy as well as strontium isotopes (Anderson et al., 2011; Bohaty et al., 2011). The key age control data are summarized here as follows. Strontium isotopes from bivalve fragments from Hole 3C (11.56 mbsf) had an $^{87}Sr/^{86}Sr$ ratio indicating middle Eocene (35.9±1.1 Ma), which is supported by diatom, nannofossil, and dinoflagellate assemblages (Bohaty et al., 2011) as well as *in situ* pollen (Warny & Askin, 2011a,b). For Hole 3C the diatom assemblage includes *K. gaster* (13.60 to 8.68 mbsf), which constrains the age to ≤~36 Ma while the presence of *P. aculeifera* limits the age to ≥34.0 Ma (13.14 to 4.57 mbsf) (Bohaty et al., 2011). This places the age of Hole 3C between 36 and 34 Ma. For Hole 12A the $^{87}Sr/^{86}Sr$ ratio indicates an age of 27.2±0.6 Ma (4.96 mbsf), the presence of diatom *C. rectus* (28.5 to 3.60 mbsf) indicates an age ≤28.4 Ma, the presence of the nannofossil *D. bisectus* (0.96 mbsf) supports an age ≥20.9 Ma, and the presence of the diatom *K. cicatricata* (4.36 to 0.30 mbsf) indicates ≥23.3 Ma placed. This implies Hole 12A dates from the late Oligocene with an age range between 28.4 and 20.9 Ma (Bohaty et al., 2011). Hole 5D was determined to be middle Miocene based on the presence of the diatom *D. ovata* (19.05 to 18.80 mbsf) as 12.1 Ma, the presence of the diatom *D. dimorpha v. areolate* (30.36 to 18.80 mbsf) suggests an age ≤12.8 Ma, and the presence of the diatom *N. denticuloides* (30.36 to 18.80 mbsf) constrains the lower limit to ≥11.7 Ma dating the sediments to 12.8-11.7 Ma (Bohaty et al., 2011) **(Figure 2A**). For the Pliocene sediment, based on the presence of *T. complicata* (16.25 to 8.95 mbsf), the age was limited to 5.1 Ma and the lack of *F. barronii* provides the lower constraint of ≥4.3 Ma (Bohaty et al., 2011), the age estimate is between 5.1 and 4.3 Ma. Based on the sediment thickness of the core sections used in this paper, these sections represent up to a few 100 kyrs of deposition (Bohaty et al., 2011).

The sediment from Hole 3C (middle Eocene) consists of muddy to very fine sand interpreted as deposited in shallow water continental shelf depositional setting (Wellner et al., 2011), Hole 12A

(late Oligocene) consists of diatomaceous mud and muddy sand determined to be a distal delta, while Hole 5D (middle Miocene/Pliocene) consists of diamict with layers of diatomaceous mud interpreted as a proximal glacimarine shelf setting for Units IV and V that span the middle Miocene section and an outer shelf environment impacted by strong bottom currents for Units II and III which is the Pliocene section (Anderson et al., 2011; Wellner et al., 2011). For this project, we followed the prior pollen sampling (Anderson et al., 2011; Warny & Askin, 2011a, 2011b), collecting 50 samples for biomarker analyses in the middle Eocene (Hole 3C, n=22), late Oligocene (Hole 12A, n=11), middle Miocene (Hole 5D, n=13) and Pliocene (Hole 5D, n=4).

3. Methods

3.1. Biomarker Extraction and Purification

Sediment samples (10 to 22 g dry weight) were freeze dried, homogenized and lipids were extracted using DIONEX Accelerated Solvent Extraction with 9:1 (*v/v*) dichloromethane (DCM) to methanol at 100°C and 1500 psi at the University of Southern California. The total lipid extract was separated into a neutral and acid fraction using a NH_2 sepra column eluted with a 2:1 (*v/v*) ratio of DCM:isopropanol (neutral fraction) and 4% formic acid in diethyl ether (acid fraction). The neutral fraction was separated over silica gel eluting alkanes with hexanes and then the polar fraction eluting first with DCM and then with methanol. The acid fraction was methylated overnight with methanol of a known isotopic concentration and hydrochloric acid (95:5) and dried using an anhydrous sodium sulfate column yielding the fatty acid methyl esters (FAMEs). The FAMEs were purified using a silica gel column: eluting first any impurities with hexane, and then collecting the FAMEs with DCM.

3.2. Liquid Chromatography Analyses

An internal C_{46} GDGT standard (Huguet et al., 2006) was added to the polar fractions containing glycerol dialkyl glycerol tetraethers (GDGTs) for quantification. These fractions were then dissolved in hexane: isopropanol (99:1) and filtered (0.45 μm PTFE) prior to injection on an Agilent 1260 High-Performance Liquid Chromatography (HPLC) coupled to an Agilent 6120 mass spectrometer at the University of Arizona. GDGTs were analyzed using two BEH HILIC silica columns (2.1×150 mm, 1.7 μm; 90 Waters) and the methodology of Hopmans et al.,

(2016). Single Ion Monitoring (SIM) of the protonated molecules ($M + H^+$ ions) was used to detect GDGTs with abundances determined by comparison to an internal standard at m/z 744, using a single standard we consider relative response factors to be semi-quantitative. We report total concentrations of branched (*br*GDGTs) and isoprenoidal (*iso*GDGTs) GDGTs in the sediments as measures of terrestrial and marine inputs respectively, and calculate the Branched and Isoprenoidal Tetraether (BIT) index:

$$BIT = \frac{Ia+IIa+IIa'+IIIa+IIIa'}{Ia+IIa+IIa'+IIIa+IIIa'+Cren} \quad \textbf{(1)}$$

where Ia, IIa and IIIa represent the abundances of both the 5′ and 6′ methyl isomers of the non-cyclic terrestrial *br*GDGTs (from soil bacteria) and Cren represents the abundance of crenarchaeol (mostly produced by marine archaea) (Hopmans et al., 2004).

In all samples, the 5-methyl *br*GDGT index, MBT'_{5Me} (de Jonge et al., 2014, Hopmans et al., 2016) was calculated as

$$MBT'_{5Me} = \frac{Ia+Ib+Ic}{Ia+Ib+Ic+IIa+IIb+IIc+IIIa+IIIb+IIIc} \quad \textbf{(2)}$$

and converted to mean annual air temperature for months above freezing (MAF) using the $BayMBT_0$ calibration (Dearing Crampton-Flood et al., 2020). The $BayMBT_0$ calibration applies Bayesian statistics to calibrate MBT'_{5Me} to MAF based on a prescribed prior mean of temperature (prior) for that region and time period studied and a prior standard deviation (Dearing Crampton-Flood et al., 2020). MAF is appropriate as soil bacteria are not thought to be active below freezing and thus *br*GDGTs are not produced and calibrations find no predictive power in months below freezing. Thus, this $BayMBT_0$ approach improves upon the BayMBT calibration to MAAT. While we do not recommend MAAT determinations as bacteria are not active in the sub-zero temperatures, we report MAAT in addition to MAF for comparison with other proxies and publications that have reported MAAT.

When applying Bayesian calibrations, prior temperatures are assigned. For the Eocene, we selected a prior of 10°C as previous studies suggest regional temperatures of 8-13°C during the middle Eocene based on weathering proxies (Passchier et al., 2013), fossil leaf assemblages (Francis et al., 2008), and bivalve oxygen isotopes (Judd et al., 2019). Temperature estimates for

the Oligocene are ~7-9°C from CIROS-1 and CRP cores from the Ross Sea (Passchier et al., 2013); therefore, a prior of 8°C was used. A prior of 7°C was used for the Miocene based on best estimates of summer temperatures from isotope-enabled climate model interpretations of plant wax δD from AND-2A from the Ross Sea (Feakins et al., 2012), summer temperatures of 5°C based on fossil data from the Dry Valleys at 14 Ma (Lewis et al., 2008), and similar temperatures from IODP Site U1356 from Wilkes Land (Passchier et al., 2013). We used a prior of 2°C for the Pliocene. In all time periods a standard deviation of ±15°C was assigned to the prior as a large uncertainty ensures that the calibration is not overly reliant on the prior for the temperature estimates (Tierney & Tingley, 2014).

In addition, the cyclization of branched tetraether (CBT') index (De Jonge et al., 2014) was calculated and used to estimate soil pH.

$$CBT' = log_{10}\left[\frac{Ic+IIa'+IIb'+IIc'+IIIa'+IIIb'+IIIc'}{Ia+IIa+IIIa}\right] \quad \textbf{(3)}$$

$$pH = 7.15 + 1.59CBT' \quad \textbf{(4)}$$

We use the $\#Rings_{tetra}$ index (Sinninghe Damsté, 2016) to assess in-sediment *br*GDGT production in shelf settings:

$$\#Rings_{tetra} = \frac{Ib+2*Ic}{Ia+Ib+Ic} \quad \textbf{(5)}$$

*Iso*GDGTs with 0–3 cyclopentane moieties (GDGT-0 to GDGT-3) and crenarchaeol (Cren) with an additional cyclohexane moiety and its regioisomer crenarchaeol′ (Cren′) are dominantly from marine archaeal production. Following (Schouten et al., 2007), TEX_{86} was calculated using the equation:

$$TEX_{86} = \frac{[GDGT-2]+[GDGT-3]+[Cren\prime]}{[GDGT-1]+[GDGT-2]+[GDGT-3]+[Cren']} \quad \textbf{(6)}$$

We converted the TEX_{86} record to mean annual sea surface temperatures (SSTs) using the BAYSPAR analogue calibration (Tierney & Tingley, 2014). This Bayesian calibration applies TEX_{86} using a prior mean temperature estimate and a large prior standard deviation to minimize error between the true values and the proxy estimated SSTs (Tierney & Tingley, 2014). We

select prior information from nearby sites from the closest time interval. The prior for the Eocene was set to 15°C based on TEX_{86}^{L} and biostratigraphy from Seymour Island (Douglas et al., 2014) and BAYSPAR and $U^{k'}_{37}$ estimates from DSDP Site 511 suggesting temperatures of 16-18°C (Houben et al., 2019; Lauretano et al., 2021). The prior used for sea surface temperature for the Oligocene was also 15°C based on TEX_{86} data from Site U1356, with SSTs around 15°C during the middle Oligocene (Hartman et al., 2018) and $U^{k'}_{37}$ estimates of 10 to 15°C around 31.5 Ma (Plancq et al., 2014) from DSDP Site 511. The Miocene prior was 12°C based on BAYSPAR TEX_{86} estimates from the Weddell Sea of 10-15°C at 11 Ma (Hartman et al., 2018) and estimates of 10-13°C from TEX_{86} and Δ_{47} from Site 1171 from the South Tasman Rise (Leutert et al., 2020). For the Pliocene the prior utilized was 5°C based on SST estimates around 4 Ma from TEX_{86}^{L} from ANDRILL AND-1B core from the Ross Sea (McKay et al., 2012) and the presence of *Leiosphaeridia* from James Ross Island suggesting SST of -2 to 5°C (Edwards et al., 1991; Salzmann et al., 2011). The standard deviation used in the reconstruction was ±10°C, a large uncertainty ensures estimated SSTs are primarily controlled by TEX_{86} values and not overly constrained by the prior mean (Tierney & Tingley, 2014). Using this standard deviation results in low sensitivity to the choice of prior, that is within the uncertainty of the calibration estimates. When comparing to regional TEX_{86} reconstructions published with earlier calibrations, we recalibrated here using BAYSPAR, with the priors as above for each time period for consistency.

Samples with a BIT>0.4 as well as samples with a delta ring index (ΔRI) >0.3 were excluded from TEX_{86} reconstruction. A high BIT indicates high terrestrial input to the site which could introduce non-thermal influences on the TEX_{86} values (Weijers et al., 2006) while a high ΔRI implies non-analogue distributions (Zhang et al., 2016), where:

$$RI_{sample} = (0[GDGT-0] + 1[GDGT-1] + 2[GDGT-2] + 3[GDGT-3] + 4[cren] + 4[cren']) \quad \textbf{(7)}$$

$$RI_{TEX} = -0.77TEX_{86} + 3.32(TEX_{86})^2 + 1.59 \quad \textbf{(8)}$$

$$\Delta RI = RI_{TEX} - RI_{sample} \quad \textbf{(9)}$$

Samples with a high methane index (MI)>0.5 are excluded from the TEX_{86} reconstruction as high MI indicate that GDGTs could be sourced from methanogenic producers which can lead to bias TEX_{86} values (Zhang et al., 2011).

$$MI = \frac{[isoGDGT-1]+[isoGDGT-2]+[isoGDGT-3]}{[isoGDGT-1]+[isoGDGT-2]+[isoGDGT-3]+[isoGDGT-5]+[isoGDGT-5']} \quad \textbf{(10)}$$

3.3. Gas Chromatography Analyses

FAMEs, alkanes and hopanes were identified by an Agilent 6890 GC equipped with a Rxi-5ms column (30 m x 0.25 mm, film thickness 0.25 μm); and a 7683 programmable injector connected to an Agilent 5973 MSD mass spectrometer and quantified by flame ionization detector (FID) at the University of Southern California. The GC run conditions for the *n*-alkanes and FAMEs started at 50ºC for 3.5 min, ramping at 20ºC/min to 300ºC and held until all compounds eluted. We reran the alkanes fraction using a slower ramp and a longer run time to achieve hopane peak separation: ramping from 50–140 °C at 20 °C/min; 140–300 °C at 4 °C/min; and 15 min hold at 300 °C. Peak areas determined by GC-FID were used for ratio calculations for *n*-alkanes and FAMEs and hopanes, *n*-alkanes and FAMEs were additionally quantified relative to an in-house standard mixture of various alkanes and FAMEs. We report the concentration of C_{20}–C_{32} *n*-alkanoic acids and C_{16}–C_{29} *n*-alkanes and calculate the summed C_{23} to C_{33} alkanes and summed C_{20} to C_{32} FAMEs in ng/gdw. The C_{16}-C_{18} are not included in the total as they are potentially sourced from contaminants based on processing blanks. We also calculate the average chain length (ACL) and carbon preference index (CPI) using the following formulae:

$$\text{ACL: } \Big/_{\sum[C_n]}^{\sum(n * [C_n])} \quad \textbf{(10)}$$

$$\text{CPI: } \Big/_{(\sum C_{n+1} + \sum C_{n-1})}^{2 \sum C_n} \quad \textbf{(11)}$$

where n is 24–32 for *n*-alkanoic acids and 23–33 for *n*-alkanes.

We also screened the alkanes fraction for the presence of hopanes, biomarkers that derive from membrane lipids in bacteria and undergo isomerization with increasing thermal maturity, using

their diagnostic mass fragments 191 m/z ion trace and published spectra (Inglis et al., 2018; Sessions et al., 2013; Uemura & Ishiwatari, 1995), and noted where those samples included a detectable uncharacterized complex mixture above baseline. Each sample was assessed for the presence of C_{27} through C_{31} hopanes and their isomers, with their relative abundance assessed by peak area determinations. Replicate measurements of standards indicate reproducibility typically better than 5%, however data quality deteriorates for the smallest peaks near detection limits. With increasing maturity, the 17β,21β(H) (ββ eq. 12) configuration changes to the 17β,21α(H) (βα eq. 12) and 17α,21β(H) (αβ eq. 12) configuration. We calculated the hopane index for each hopane present as follows:

$$hopane\ index = \frac{\beta\beta}{(\alpha\beta+\beta\alpha+\beta\beta)} \quad \textbf{(12)}$$

4. Results

The results of the published sedimentology, chronology, and palynology efforts are summarized in **Figure 2a-d** (Anderson et al., 2011, Bohaty et al., 2011) to provide the depositional context for the proxy data. The pebble evidence for ice rafting and the pollen evidence for vegetation and reworking (**Figure 2c and d**; Anderson et al., 2011) are particularly relevant context for the biomarker data generated in this study. Our biomarker results are organized by evidence for maturity, biomarker ratios and indices, biomarker concentrations and temperature inferences (**Figure 2e-k**).

4.1. GDGTs

4.1.1. BIT

GDGTs were detected and quantified in all 50 samples. We use the BIT index as a measure of the proportional input of *br*GDGTs to *iso*GDGTs. We find BIT decreases from the Eocene to Pliocene sections (**Figure 2g**). The middle Eocene section has an average BIT index of 0.65 with a range from 0.57 to 0.74 (n=22). The late Oligocene section has an average of 0.35 and ranges from 0.09 to 0.57 (n=11). The middle Miocene section has an average BIT of 0.27 ranging from 0.09 to 0.40 (n=13). The Pliocene section has average values of 0.09 only varying between 0.08-0.10 (n=4). Decreasing BIT values from the Eocene to the Pliocene could be consistent with

increased marine production of *iso*GDGTs and/or decreased flux of terrestrial soil-derived *br*GDGTs to the marine margins.

4.1.2. *Br*GDGTs

Σ*br*GDGT concentrations ranged from 0.1 to 10.3 to ng/gdw (mean 2.1 ng/gdw, n=50). The concentrations decrease from the Eocene to Pliocene (**Figure 2j**): ranging from 2.2 to 10.3 ng/gdw (mean 4.5 ng/gdw, n=22) in the Eocene; from 0.7 to 2.9 ng/gdw (mean 1.9 ng/gdw, n=11) in the Oligocene; from 0.1 to 3.3 ng/gdw (mean 1.5 ng/gdw, n=13) in the Miocene, and the Pliocene had the lowest concentrations ranging from 0.5-0.7 ng/gdw (mean 0.64 ng/gdw, n=4). Sedimentology indicates increased sand and pebble components, which can dilute the biomarkers, however the *n*-alkyl lipids and *iso*GDGTs increase in concentration, thus their productivity or input fluxes overwhelm any dilution effect. Whereas we see a reduced flux of soil bacterial *br*GDGTs compounds likely due to the reduced area for soils as glaciation proceeds, and the cooling trend that reduces the months above freezing for bacterial growth. In these coastal shelf sediments, we checked for *in situ* production of brGDGTs using $\#Rings_{tetra}$, finding values typically of 0.2 (no concern of in-sediment bacterial production), with a few samples reaching 0.4 (in samples with low BIT). Overall $\#Rings_{tetra}$ has no correlation with MBT'_{5Me}, allowing us to discount any significant marine overprinting of the land temperature proxy here.

MBT'_{5Me}-based temperatures were calculated for all 50 samples (**Figure 2k**). Reconstructed MAF were consistent across SHALDRIL sediments from the late Eocene (11.5±0.4°C, mean, 1σ, n=22), Oligocene (12.5±0.7°C, n=11) and Miocene (11.1±1.2°C, n=13); with lower temperatures in the Pliocene (5.4±1.1°C, n=4), that are significantly different with respect to calibration uncertainties (shading on **Figure 2k**) on the order of 4°C (1σ). MAAT estimates display similar trends to MAF reconstructions, as expected since the proxy contains no sub-zero sensitivity. By inclusion of the colder months in the calibration, the MAAT estimates are offset by approximately 5°C cooler to the MAF estimates.

Soil pH calculated from CBT′ averaged 6.3±0.4 (1σ, n=50) and is thus remarkably stable. The highest pH values (~7) are found at the top Oligocene sample and several Miocene samples as well as the four Pliocene samples (not shown) consistent with aridity, although the modest difference is within calibration uncertainty and is not shown or interpreted further.

4.1.3. *Iso*GDGTs

Σ*iso*GDGT concentrations ranged from 1.1 to 16.0 ng/gdw (mean 7.7 ng/gdw, n=50) overall (**Figure 2j**). Concentrations in the Eocene ranged from to 4.1 to 14.8 ng/gdw (mean 7.1 ng/gdw); in the Oligocene from 3.7 to 13.2 ng/gdw (mean 8.1 ng/gdw); and in the Miocene section ranges from 1.1 to 13.2 ng/gdw (mean 7.4 ng/gdw). The Pliocene has the maximum concentration of Σ*iso*GDGTs with a range from 6.4 to 16.0 ng/gdw (mean 10.2 ng/gdw) despite sedimentary dilution by pebbles and sand (**Figure 2b and c**), likely implying increased ocean productivity.

We track *iso*GDGT distributions for signals that may confound temperature interpretations. For example, high ΔRI indicates microbial lipid distributions different to those of the open ocean today, often associated with high BIT indicating high terrestrial inputs. Out of 50 samples, high ΔRI (>0.3) resulted in exclusion of 32 samples from consideration (many of which also had high BIT), and high BIT (>0.5) resulted in the exclusion of 2 additional samples. Additional checks were for methane cycling communities as detected by the MI index. The MI was below 0.5 for all samples except for two that also had high ΔRI and were excluded from the SST calculations. Only 16 samples had *iso*GDGT distributions where TEX_{86} values were viable for SST reconstruction.

Eocene SSTs were not generated due to high BIT and ΔRI values. Limited Oligocene SSTs passed the criteria, but where BAYSPAR could be applied, SST ranged between 11.6 and 6.4°C (mean 9.6 ±2.8°C, 1σ, n=3). Miocene SSTs ranged from 14.3 to 3.9 °C (mean 10.2±3.4°C, n=10). Pliocene SSTs were considerably colder (2.8±0.9°C, n=3) with only 1 sample excluded for the Pliocene due to reduced terrestrial flux of Σ*br*GDGTs. Calibration uncertainty for all temperature estimates is on the order of 4°C (1σ), rigorously determined by Bayesian methods and illustrated by shading (**Figure 2k**).

4.2. Alkyl lipids

4.2.1. Alkanoic acids

n-Alkanoic acids were detected from C_{16} to C_{32} (n=32); however, C_{16} to C_{19} were excluded as possible contaminants present in processed blanks and are therefore not reported or further

discussed. The concentration of *n*-alkanoic acids (C_{20} to C_{32}) ranged from 0 to 3650 ng/gdw with an average value of 1625 ng/gdw (**Figure 2i**). The lowest concentrations 0 and 7 ng/gdw occur in the two youngest Pliocene samples. The additional two Pliocene samples have concentrations of 211 and 482 ng/gdw. Except for two Miocene samples from Hole 5D at 22.3 mbsf and 25.2 mbsf, all other samples exceed 500 ng/gdw with average values of 1894 and 1950 ng/gdw for the Miocene and Oligocene respectively. Only three samples from the Eocene were able to be quantified with an average *n*-alkanoic acid concentration of 1203 ng/gdw. The CPI ranged from 3.6 to 9.7 with an average value of 5.3 across the record. The average Pliocene CPI was 4.1 based on the two samples that contained long chain *n*-alkanoic acids, Miocene 6.0, Oligocene 6.0, and Eocene 4.6. ACL ranged from 26.0 to 28.5 with an average of 27.8 with the highest average ACL from the Eocene at 28.2, the other three timeslices have average ACLs from 26.9-27.5. Molecular abundance distributions display C_{26} and C_{28} co-dominance (**Figure S2**).

4.2.2. Alkanes

The *n*-alkanes were detected from C_{17} to C_{31} (n=49) with concentrations ranging from 119 to 1904 ng/gdw (mean 768 ng/gdw). Summed long chain *n*-alkanes (C_{23} to C_{31}) ranged from 87 to 1822 ng/gdw (mean 607 ng/gdw, **Figure 2i**). The Pliocene samples have an average concentration of long chain *n*-alkanes of 140 ng/gdw with the Miocene and Oligocene averaging 542 and 414 ng/gdw respectively. The CPI varied from 1.3 (mature) to 4.6 (immature) (mean 2.6) (**Figure 2f**). CPI varied between timeslices, Eocene (3.6), the Oligocene (1.9), Miocene (2.1) and Pliocene (1.5). The ACL ranged from 25.9 to 28.1 with an average value of 27.2. The Eocene had the highest ACL of 27.9 with the Oligocene averaging 26.5, the Miocene 26.8 and the Pliocene 26.6 indicating a tendency to shorter chain lengths after the Eocene (**Figure 2h**). A hierarchical cluster analysis using Euclidean distance was performed on the *n*-alkane chain length distribution after normalizing to assess changes in inputs such as reworking. The clustering analysis divided the sample set into 3 groups (**Figure S3**), with clusters 2 and 3 showing presence of shorter chain compounds ($<C_{23}$), without odd-over-even carbon preference, i.e., diagnostic of mature *n*-alkanes. The typical plant-like odd-over-even predominance can be seen ($>C_{24}$) in all clusters.

4.2.3. Hopanes

Hopanes were detected in all samples; however, not all hopanes (C_{27}-C_{31}) were detected in the Pliocene samples. To be able to compare across all samples we report the average hopane ratio across all hopanes detected (hereafter hopane ratio). The Eocene section (Hole 3C) has an average hopane ratio of 0.43 (0.25 to 0.53) indicating moderate maturity, with the most mature values found at the top of the section. The Oligocene samples (Hole 12A) have an average hopane index of 0.26 (0.20 to 0.29). The Miocene samples have an average value of 0.28 (0.09 to 0.34). Hopanes were detected across a limited range in the Pliocene samples compared to the other SHALDRIL II samples. Pliocene samples with an average value of 0.20 (0.03 to 0.34) include samples with high thermal maturity. The hopanes signify moderate maturity overall, with increasing thermal maturity in the younger sections (**Figure 2e**).

5. Discussion

5.1. Eocene

SHALDRIL II Hole 3C provides a snapshot of late Eocene climate. Our new *br*GDGT-based temperature reconstruction using $BayMBT_0$ estimates MAF temperatures of 11.5±0.4°C (n=46) during the late Eocene (**Figure 2k**) presumably reflecting conditions on the adjacent tip of the Antarctic Peninsula. Since winter temperatures are not recorded by microbial growth, we do not recommend the MAAT BayMBT calibration, however we do provide those estimates for comparison purposes (**Figure 2k**). These values are similar to mean annual air temperature estimates based on climate leaf analysis multivariate program (CLAMP) analyses from nearby Seymour Island of ~11°C (Francis et al., 2008) with unquantified uncertainty of several degrees, summer temperature estimates from the La Meseta Formation on Seymour Island of >10°C based on pollen (Warny et al., 2019), mean annual temperature estimates of 11-16°C from the Weddell Sea ODP Site 696 (Thompson et al., 2022), and mean annual temperature estimates from King George Island of 12-13°C from coexistence analysis of fossil floras (Hunt & Poole, 2003; Poole et al., 2005). Based on the oxygen isotopes on shallow marine bivalves the seasonal cycle for nearby Seymour Island during the middle Eocene is estimated to be 8°C (Judd et al., 2019); if coastal land temperature seasonality is similar to that recorded by shallow marine bivalves, this would imply winter temperatures of about 3°C. Based on the air temperatures from other proxies and the seasonal cycle for nearby Seymour Island, Eocene temperatures are likely

above freezing year round (i.e., MAF = MAAT) on the Antarctic Peninsula. Pollen from two different locations on King George Island on the Antarctic Peninsula suggest MAAT of 11-15°C (mean of 12°C) and 9-27°C (mean 13.3°C) (Hunt & Poole, 2003; Poole et al., 2005). The SHALDRIL reconstructions reasonably fall between estimates from higher and lower latitudes, being warmer than MAAT estimates of 8-10°C from weathering proxies in the Ross Sea (Passchier et al., 2013) and within pollen estimates (8-18°C) from the Weddell Sea sector (Houben et al., 2011; Mohr, 1990; Pound & Salzmann, 2017).

SST estimates were not generated for the Eocene SHALDRIL sediments due to BIT>0.4 and ΔRI>0.3 suggesting strong fluxes of terrestrial inputs to this site that would preclude reliable SST estimates. However, TEX_{86} measurements from the La Meseta Formation on nearby Seymour Island (Douglas et al., 2014) are recalibrated using BAYSPAR here to yield SST estimates of 11.3-13.5°C). Clumped isotope measurements on shallow marine bivalves at the same site indicate temperatures of 11-17°C (Douglas et al., 2014). Another record from Seymour Island used the chemical weathering of minerals and determined a chemical index of alteration (CIA) <60 and increasing illite mineralogy to reveal conditions on land (Dingle et al., 1998) suggesting a cool and wet climate shifting to a cold relatively dry environment in the late Eocene.

In the uppermost 4 samples of Hole 3C, a decline in *N. fusca* pollen abundance (**Figure 2d**) suggests the recovered sediments capture the first signs of decreasing temperature and deteriorating conditions for plants on the Antarctic Peninsula, although the EOT was not recovered (Anderson et al., 2011). Compound specific isotopic analysis of the same Eocene section similarly found lower δD values in the same samples (Feakins et al., 2014), compared to downcore samples within 3C, tentatively interpreted as drying associated with cooling. The increased proportion of reworked pollen is likely indicative of glacial erosion which would require cooling and drying conditions suggested by the δD values. In the same horizon, we report declines in the hopane index (**Figure 2e**) and *n*-alkane CPI (**Figure 2f**), which both suggest more thermally mature inputs from older sediments coinciding with increasing reworked pollen. In addition, the *n*-alkane chain length distribution for the uppermost samples in 3C are in alkane cluster 3 (**Figure S3**), showing more mature inputs compared to the earlier samples within 3C. The cluster analysis indicates that the mature signature in the late Eocene samples is

similar to the reworked mature components found in the Miocene and Pliocene of Hole 5D. The low *n*-alkane CPI and hopane index could be interpreted as thermal heating; however, the presence of non-mature biomarkers (e.g., *n*-alkanoic acids with CPIs>1 and the presence of GDGTs) as well as well-preserved pollen rules out *in situ* heating (ct. Duffy et al., 2022; Tibbett et al., 2021). The declining CPI and hopane index instead indicates increased reworking, likely initial signs of glacial expansion and transport to the site, presumably from distal iceberg rafting (pebbles appear, **Figure 2c**) or local fluvial erosion.

5.2. Oligocene

We see signs that fluvio-glacial erosion increased during the Oligocene, as we find biomarker evidence for more reworked inputs based on the reworked pollen percentage, the hopane index and the alkane CPI (**Figure 2d-f**) relative to the earlier Eocene section. This is consistent with the presence of sand grains with glacially-derived high-stress microtextures indicating expanding Alpine-style glaciation (Kirshner & Anderson, 2011). Although there is reworking, we do not expect contributions of *br*GDGTs from sediments of such maturity (hopane index approaches 0). In addition, we note the presence of immature material (including *n*-alkanoic acids and pollen) and no change in the concentration of GDGTs associated with changes in the hopane index and CPI. From the Eocene (Hole 3C) to Oligocene (Hole 12A), the concentration of *n*-alkyl lipids and *br*GDGT decreases, and the BIT decreases. The declining terrestrial contribution may be related to a decline in terrestrial production by plants and soil bacteria, however temperatures do not drop at the same time making this unlikely. Instead, the likely explanation is the greater distance from the coastline (~100 km further), reducing the terrestrial flux. The plateau position of Hole 12A, ~100 m shallower water depth today relative to 3C, may also reduce the terrestrial delivery however paleodepth may have been deeper based on diatoms (Bohaty et al., 2011). Biomarker assemblages remain consistent with interpretations that *iso*- and *br*GDGTs are penecontemporary with the *iso*GDGTs mainly produced in the water column and the *br*GDGTs dominated by soil inputs likely from local fluvial runoff from the Antarctic Peninsula. On land, *br*GDGT reconstructed air temperatures for MAF range from 13.3 to 10.8°C (mean 12.5±0.7°C, n=11) similar to Eocene MAF temperatures, suggesting that the change in sampling location and possible reduction in terrigenous flux has not biased the temperature signal carried. Pollen assemblage based estimates from nearby Seymour Island suggests MAAT between 8-18°C with

warm month mean temperatures of 17-24°C (Pound & Salzmann, 2017;Warny et al., 2019) and pollen MAAT estimates. These estimates overlap with the Oligocene temperatures reconstructed here. Pollen MAAT estimates from the Antarctic Peninsula (40 Ma) suggest temperatures of 11-15°C (Francis et al., 2008; Poole et al., 2005). These temperature records from the Eocene and Oligocene are similar further indicating minimal change in temperature on the Antarctic Peninsula from the Eocene to Oligocene.

In contrast, the weathering S-index from CRP-3 from the Ross Sea (derived from Transantarctic Mountains) suggests ~8°C for the middle to late Oligocene, a decrease of 3°C from the Eocene (Francis et al., 2008; Passchier et al., 2013) indicating substantial cooling in the continental interior. Although an ice sheet was present on Antarctica during the Oligocene (Levy et al., 2019), our reconstructions find little change in the months above freezing temperatures recorded by *br*GDGTs on the tip of the Antarctic Peninsula, at the northerly limit of the continent.

Diatom assemblages from SHALDRIL II show a less diverse assemblage and smaller taxa in the Oligocene core, which may indicate cooling and a deeper paleowater depth for Hole 12A, although modern depth is 100 m shallower, and/or local surface cooling from the Eocene to Oligocene (Bohaty et al., 2011). The winter-season included sea ice based on the presence of penecontemporary dinoflagellate cysts and acritarchs in 12A (Warny & Askin, 2011a). High BIT and ΔRI meant we were not able to estimate any Eocene and limited Oligocene SSTs so we do not have independent evidence for SST cooling. Where BAYSPAR could be applied to Oligocene samples dating from ~27 Ma, SST reconstructions ranged between 11.6 and 6.4°C (mean 9.6±2.8°C, n=3; **Figure 2e**).

There are limited Oligocene SST records in the region, with none overlapping 27 Ma results from SHALDRIL, however we review bracketing data for 34-32 Ma and 24-23 Ma. Nearby on Seymour Island, clumped isotope paleothermometry on bivalves yields estimates of 9, 13 and 17°C for three specimens from the same stratum leaving uncertainty around shallow ocean waters temperatures at 34 Ma, and in the same sample, TEX_{86} recalibrated with BAYSPAR suggests 13.5°C (Douglas et al., 2014). Further north from DSDP Site 511 near the Falkland Plateau, SST estimates for 34-32 Ma average 13±3.3°C (n=32) from TEX_{86} BAYSPAR and 11±1.4°C (n=28) from $U^{k'}_{37}$, the latter may be cold-biased due to advection (Houben et al., 2019;

Lauretano et al., 2021). At the same time, 33-32 Ma, Maud Rise ODP Site 689, to the East of the Weddell Sea, yielded clumped isotope SST estimates of 12±3.1°C (n=5) (Petersen & Schrag, 2015). In younger sediments, DSDP Site 269 off Wilkes Land, East Antarctica, TEX_{86} values for 24.2-23 Ma, recalibrated with BAYSPAR here, yield comparable SSTs (13±3.3°C, n=13). These SST records from the early, mid (this study) and late Oligocene suggest minimal SST cooling in the Weddell Sea sector. While detailed evidence for the climate of the Oligocene remains geographically and temporally limited, our results from SHALDRIL for 27 Ma add to earlier reports of Oligocene Southern Ocean warmth (O'Brien et al., 2020).

5.3. Miocene

Penecontemporary pollen from SHALDRIL II suggest austral summer temperatures of 10°C on the tip of the Antarctic Peninsula during the latter portion of the middle Miocene (12.8-11.7 Ma), likely a low shrubby tundra environment (Anderson et al., 2011). Reworked pollen proportions increase from the Oligocene to Miocene (**Figure 2d**). The low hopane index and *n*-alkane CPI around 1 indicate reworked material was delivered to the Miocene horizons of Hole 5D, in addition to the continued presence of fresh pollen and *n*-alkanoic acids indicating that the sedimentary organics contain a mixture of penecontemporary inputs and transported, mature, reworked materials. An increased prevalence of pebble-sized dropstones in these Miocene sediments (**Figure 2c**) indicates a dramatic increase in glaciers with a marine-terminating calving margin relative to the Oligocene (Wellner et al., 2011). The pebbly-gray diamicton has been described as a proximal glacimarine setting, with ice on the peninsula as well as Joinville Island (Wellner et al., 2011). Thus iceberg-rafted sediment delivery can derive from the newly glaciated nearby peninsula. Yet clay mineralogy found no change in source area or weathering regime (Wellner et al., 2011), thus the dominant sourcing may be dominantly marine-terminating valley glaciers from the WAIS/EAIS coastlines bordering the Weddell Sea as in the Oligocene and Eocene (Carter et al., 2017). This is consistent with changes in sand grain morphology in the Miocene section of the SHALDRIL cores that indicate a change towards large-scale ice sheets, rather than individual valley glaciers (Kirshner & Anderson, 2011). We thus suggest the increase in reworked pollen and biomarker indices (CPI, hopane) is associated with enhanced iceberg calving from EAIS/WAIS during the middle Miocene. By the late Miocene the Antarctic Peninsula Ice sheet (Bart et al., 2005; Davies et al., 2012) had expanded onto the northern

Antarctic Peninsula continental shelf (Smith & Anderson, 2010). However, in the time period sampled, glaciation was still contained on the Peninsula nearby and the site was underwater as indicated by microfossil (diatom) and biomarker input from marine productivity.

The concentrations of *n*-alkanoic acids, *iso*GDGTs and *br*GDGTs increase within the Miocene sediments suggesting high productivity and/or preservation (**Figure 2i and j**). High organic content, a sulfurous smell on core splitting and no bioturbation in Hole 5D (Miocene and Pliocene sections) suggests low oxygen conditions (Wellner et al., 2011) conducive to preservation of biomarkers, relative to the earlier sections recovered. However, within the same core section changes in GDGT concentrations may denote changes in productivity. Both *br*- and *iso*GDGT concentrations increase within the Miocene core. BIT increases slightly (**Figure 2g**) due to the increase in *br*GDGT concentrations even though their absolute concentrations remain much lower than *iso*GDGTs. The increased *iso*GDGT concentration also suggests an increase in ocean productivity by Archaea (used for the TEX_{86} temperature proxy). In high organic, shelf settings there may be some in-sediment production of *br*GDGTs (Sinninghe Damsté, 2016). We tested for this concern but found just 5 of the 11 samples have elevated $\#Rings_{tetra}$ of 0.4 versus 0.2 for the others, without any temperature covariation, allowing us to discount this concern. Shelf sediment *br*GDGT production is not likely to bias applications of the MBT'_{5Me} proxy here.

We find *br*GDGTs from SHALDRIL sediments dated to 12.8 to 11.7 Ma yield mean MAF of 11.1±1.2°C (1σ, n=13). While these are relatively warm temperatures they reflect the months above freezing (likely only summer months in the Miocene) when soils on unglaciated landscapes are thawed and microbial communities are active – likely exported by summer rain and fluvioglacial erosion by meltwater streams. Additional air temperature records spanning the estimated ages for the SHALDRIL are limited; therefore, we discuss air temperature records throughout the Miocene here. On the other side of the Weddell Sea, at IODP Site U1356A (~60°S paleolatitude), the MBT/CBT method estimated Miocene Wilkes Land MAT as 12°C for 16.3 to 13.8 Ma (Sangiorgi et al., 2018), although inorganic geochemistry estimates from the S-index were cooler (8°C) for 16.5 to 13.5 Ma (Passchier et al., 2013), records that include the warmth of the Miocene Climatic Optimum (MCO) and the middle Miocene Climatic Transition (MMCT). Further afield in the Dry Valleys (77°S, 1.35-1.5 km asl) in the Transantarctic Mountains – an area that remains unglaciated today - cypridoidean ostracodes and lathridiid

beetle fossils yield summer temperatures of 5°C at 14 Ma during the MCO (Lewis et al., 2008). Offshore in the Ross Sea, ANDRILL-2/2A marine sediments yielded plant wax δD, interpreted with isotope-enabled climate model experiments, to suggest MCO summer temperatures of 7°C on land (Feakins et al., 2012), consistent with palynology evidence for brief pulses of warming (Warny et al., 2009). Yet even these warm spikes during the widely-recognized warmth of the MCO, were not as warm as the temperatures recorded here (~11°C) from the more northerly latitude tip of the Antarctic Peninsula after the MMCT cooling in the latter part of the middle Miocene (12.8 to 11.7 Ma).

We now turn to middle Miocene oceanic conditions. Our TEX_{86} data (n=10) from SHALDRIL II Hole 5D indicate (late) middle Miocene (12.8-11.7 Ma) mean SSTs of 10.2±3.4°C (1σ, n=10). This is comparable with regional SST reconstructions slightly earlier in the middle Miocene spanning the MCO (14.2-13.3 Ma) at IODP Site U1356 (60°S) in the Weddell Sea, where TEX_{86} BAYSPAR estimates indicates SSTs of 12±3°C (1σ, n=10) spanning 13.8 to 10.8 Ma (Hartman et al., 2018). Similarly, a little further east and further offshore ODP Site 1171 (55°S) on the South Tasman Rise yields SSTs of 22.6±2.5°C (1σ, n=106) for 15.3-12.0 Ma based on TEX_{86} BAYSPAR (Leutert et al., 2020). SSTs have also been reconstructed at IODP Site 1171 based on clumped isotopes measured on planktonic foraminiferal calcite yielding 12.7±1.1°C (1σ, n=13) (Leutert et al., 2020). In addition, TEX_{86} from ANDRILL-2A from the Ross Sea (Levy et al., 2016) recalibrated with BAYSPAR, yields SST estimates of ~11°C (6-26°C) spanning from 20 to 11 Ma. Other proxies provide a seasonal signal. Diatom assemblages from SHALDRIL cores suggest the presence of winter-season sea ice in the northwestern Weddell Sea (Bohaty et al., 2011). The surge in the number of iceberg-rafted dropstone pebbles in these Miocene sediments in Hole 5D (**Figure 2c**) indicates a contrast between active calving from marine-terminating glaciers (WAIS/EAIS and the Antarctic Peninsula) and warm summer open water conditions offshore in the middle Miocene, and summer warmth on land.

5.4. Pliocene

Our TEX_{86}-based BAYSPAR estimates of Pliocene SSTs range from 3.3 to 1.8°C (mean 2.8±1.1°C, n=3). Diatom assemblages from the same core (Hole 5D) suggests the presence of seasonal sea ice (Bohaty et al., 2011) which is further corroborated by the presence of the

593 acritarch *Leiosphaeridia* from James Ross Island (Salzmann et al., 2011) which is found in high
594 abundance in regions with sea ice and is an indicator for the presence of sea ice (Mudie, 1992;
595 Warny et al., 2006). Other estimates from ANDRILL-1B (Ross Sea) suggest SSTs of 3-8°C (4.6
596 to 3.4 Ma) based on diatom assemblage (McKay et al., 2012). SSTs were also calculated with
597 TEX^{L}_{86} prior to 3.4 Ma (McKay et al., 2012) and were recalibrated here using BAYSPAR
598 suggesting temperatures of 8 to 18°C. There was no palynological evidence of vegetation on the
599 Antarctic Peninsula during the Pliocene (Anderson et al., 2011) reflecting the cold climate and
600 glaciation. The high proportion of reworked pollen, biomarker evidence carrying signals of
601 maturity (particularly the hopane index and alkane CPI), suggest fluvio-glacial erosion of older
602 strata locally on the Antarctic Peninsula or from the Weddell Sea margins of WAIS and EAIS by
603 icebergs (see **Section 5.5**). The Pliocene section for Hole 5D was interpreted as an outer shelf
604 environment which is supported by the lowest *n*-alkanoic acids concentration (112-482 ng/gdw),
605 *br*GDGT concentrations (0.6 ng/gdw) and the highest *iso*GDGT concentration of 10.2 ng/gdw.
606 The lower terrestrial sourced material could suggest lower inputs due to the presence of the
607 Antarctic Peninsula Ice Sheet as well as the shift from a proximal glacimarine shelf environment
608 during the Miocene to a further offshore depositional environment influenced by bottom currents
609 during the Pliocene.

610 There is winter sea ice present in this region in the Pliocene as indicated by sea-ice proximal
611 species from the same cores (Anderson et al, 2011, Bohaty et al., 2011). Increased glacial erosion
612 is apparent from glacial deposits on land (Marenssi et al., 2010) and glacial strata in the James
613 Ross Basin (Smith & Anderson, 2010). Glacial erosion from land is clearly evident from the
614 presence of dropstones (Anderson et al., 2011; **Figure 2c**) and we find clear evidence for
615 reworked deposits based on the pollen, low CPI alkanes and hopane index in the Pliocene
616 samples compared to other time slices from SHALDRIL II. Both time periods are found within
617 the same Hole 5D so there are no concerns about the site of deposition, with material expected to
618 still be delivered from the proximal, glaciated peninsula. However, icebergs may also have been
619 delivering material from around the Weddell Sea for all the time periods when pebbles are
620 present (Anderson et al., 2011).

621 In the Pliocene horizons of Hole 5D the *br*GDGTs yield MAF estimates ranging from 6.5 to
622 3.8°C (mean 5.4±1°C), capturing cooling relative to the Miocene, consistent with earlier

reconstructions of local glacial expansion on the Antarctic Peninsula, on Joinville Island and onto the Joinville Plateau (Wellner et al., 2011). We see considerable cooling in the Pliocene age soil-derived proxy, relative to the earlier times, however the microbial recorder cannot capture deepening winter cold as soil microbial activity is limited to the months when the soil thaws. The nature of the recorder also changes over time, as climate cools the amount of time that soil temperature remains above freezing decreases and is limited to the shorter summer. In addition, exposed soils are only present during interglacials and this soil bacterial biomarker proxy would not detect times of glaciated land, and this means that the reconstructed summer/interglacial temperatures for the Pliocene are likely an upper bound. These warm temperatures fit with evidence for instability of WAIS during the Pliocene from the Amundsen Sea sector sampled by IODP Exp 379 (Gohl et al., 2021).

Conditions cooled further from the Pliocene into the Pleistocene glacials, consistent with a proximal glacier on the Joinville Plateau. In the present interglacial (the Holocene), just two months, December and January have average temperatures above freezing (mean 1.1°C), with MAT of -4.6°C from Esperanza Base from 1981 to 2010, for the Antarctic Peninsula (Turner et al., 2020). Pliocene MAF reconstructed by brGDGTs (mean 5.4±1°C) are 4.3°C warmer than historical instrumental climatology MAF of 1.1°C for 1981-2010. Although a heatwave of 18.3°C was recorded at Esperanza Base in February 2020 (Francelino et al., 2021), with recurring heatwaves in 2022, showing signs of current warming.

5.5. Glacial erosion and the provenance of biomarkers

In the upper few samples of the Eocene, as well as in the Oligocene, Miocene and Pliocene, we see evidence for reworked biomarkers (based on the high CPI alkanes and the low hopane ratio) and reworked pollen in the same horizons as the pebbles (**Figure 2**). The presence of iceberg-delivered pebbles in Eocene-Pliocene age sediments in the studied sections of SHALDRIL II sediments (**Figure 2c**) and the location of the drill sites in “iceberg alley” in the Weddell Sea, implies pebbles could have been delivered by ice that calved from any margin around the Weddell Sea, which includes both EAIS and WAIS (Anderson et al., 2011; Carter et al., 2017). Iceberg alley is a major route for WAIS and EAIS derived icebergs via the Weddell gyre circulation in the modern ocean (**Figure 1**), a circulation and iceberg transit route that has likely

been in place since at least the late Eocene (Carter et al., 2017). Additional studies of this region have shown that, in the late Eocene, there was widespread ice that extended from the mountainous interiors to the coastal areas fringing the southern Weddell Sea and EAIS that have been identified in provenance studies for the Eocene noted from ODP Site 696 (water depth of 650 m) near the South Orkney Microcontinent (Carter et al., 2017). Due to this transport, distally sourced terrestrial biomarkers from both WAIS and EAIS can be deposited at the core sites. This implies distal transport of mature sedimentary organics, rafted by ice. Later, once the Antarctic Peninsula Ice Cap develops, in the Miocene and Pliocene (Wellner et al., 2011) then local iceberg generation may also transport reworked material. We do not however infer distal sourcing of the soil-derived *br*GDGTs or fatty acids. The maturity of the reworked material, means that these compounds would not be preserved in the eroding sediments, and thus we infer that the fatty acids and *b*rGDGTs are not reworked from older strata, but are penecontemporary and more locally sourced by fluvial processes from unglaciated areas of the Antarctic Peninsula.

When considering iceberg transport, the warm SSTs reconstructed in this study present a contrast. Paleotemperature reconstructions from this study and other studies (e.g., Douglas et al., 2014) suggest warm (above freezing) SSTs at the margins of the Antarctic Peninsula (**Figure 3**). Given that warm SSTs would have melted icebergs rapidly, the presence of iceberg-rafted pebbles at the tip of the Antarctic Peninsula is an apparent paradox (Douglas et al., 2014; Carter et al., 2017). Those prior estimates of warm Eocene temperature are corroborated with our new data with warm land temperatures in the Eocene and warm SSTs persisting across the Oligocene and Miocene, adding more confidence to the interpretation of icebergs calving into a relatively warm ocean, from the Eocene to the Miocene, with a vigorous Weddell Gyre current transporting the icebergs to the tip of the peninsula before they melt. This ocean circulation is supported by ocean modelling studies (Bijl et al., 2011; Goldner et al., 2014) and the paleotemperature proxies (Anderson et al., 2011; Douglas et al., 2014; Carter et al., 2017; and this study).

5.6. Implications for Cenozoic cooling

The global Cenozoic cooling trend is often described using benthic foraminiferal calcite $\delta^{18}O$ (Westerhold et al., 2020), which records glacial ice volume as well as deep ocean cooling. That trend is broadly linked to the decline in atmospheric pCO_2 and glacial ice albedo feedbacks

(**Figure 3d**). There is a transition from ~1000 ppmv in the Eocene to ~400 ppmv during the middle Miocene and Pliocene (Rae et al., 2021) reconstructed from alkenone (Badger et al., 2019; Pagani et al., 2005, 2010, 2011; Zhang et al., 2013) and boron isotope proxies (Anagnostou et al., 2016, 2020; Badger et al., 2013; Foster et al., 2012; Greenop et al., 2014, 2019; Henehan et al., 2020; Pearson et al., 2009; Sosdian et al., 2018). However, mismatches between deep ocean $\delta^{18}O$ and pCO_2 have been noted, with Oligocene warmth presenting a conundrum (O'Brien et al., 2020). Progress on separating deep ocean temperature and ice volume variables, using Mg/Ca (Lear et al., 2000, 2015) and later using clumped isotope paleothermometry, found warm deep ocean temperatures persist longer than thought, with temperatures of 5-10°C recorded across the Oligocene and Miocene(Meckler et al., 2022). Antarctic temperature reconstructions are vital to understand local climate-cryosphere coupling; however, accessing sedimentary archives remains challenging (e.g., McKay et al., 2022). Many previously collected cores can be revisited with newer techniques to make full use of the recovered sediments (e.g., Tibbett et al., 2021). Here we provide organic-biomarker based temperature constraints for land and sea at the tip of the Antarctic Peninsula for snapshots in time recovered by SHALDRIL II, which we compare to conditions on and around Antarctica and the global trend (**Figure 3**).

The tip of the Antarctic Peninsula is far from the nucleation of initial glaciations, e.g., on the Gamburtsev Mountains (Rose et al., 2013), and was likely late to respond to continental cooling, although local cooling is expected. Pollen from SHALDRIL samples indicate that *N. fusca* decline within the Eocene (Anderson et al., 2011), well before we detect a temperature change with soil biomarkers proxies here (**Figure 2**). Soil biomarkers carry no detectable (<1°C) difference in the reconstructed land temperatures for MAF from *br*GDGTs between the Eocene, Oligocene and Miocene, with any cooling between segments within the variability in each segment (**Figure 3**). Likely declining winter temperatures shortened the summer season, but *br*GDGTs only allow us to see that the temperatures remained similar in summer months. Soil biomarkers first record a cooling for MAF between the Miocene and Pliocene from 11 to 5°C. We hypothesize warm season temperatures remain similar for much of the record before the summer months finally cool in the Pliocene. In contrast, plant growth is limited much sooner as winter cooling develops in the late Eocene, shortening plants' growing season. Once local glaciation develops, the formation and microbial activity within soils would also be biased to the

interglacials, thus soil biomarker temperatures should be considered an upper bound seasonally and across orbital cyclicity.

SHALDRIL sedimentary samples have yielded evidence for cooling of ocean waters between the Eocene and Oligocene: diatom assemblages indicate cooling (Bohaty et al., 2011) and dinoflagellates and acritarchs indicate an increase in sea ice (Warny & Askin, 2011a). This cooling and sea ice formation would have aided Antarctic bottom water formation and marked an initial increase in deep ocean ventilation at the EOT (Goldner et al., 2014). Using the TEX_{86} paleothermometer, we were unable to reconstruct Eocene SSTs due to the proximal core site location and terrestrial flux of biomarkers (high BIT). From a more distal site, we were able to reconstruct Oligocene SSTs from 3 samples, finding considerable variability between 11.6 and 6.4°C with an average SST of 10°C. Miocene SSTs were available for all samples (10.2±3.4°C, 1σ, n=10), indicating that from the Oligocene to Miocene there was no clear drop in SSTs in the recovered sedimentary material. Intriguingly, deep ocean temperatures (Meckler et al., 2022) also do not show much change across this time suggesting that this may be a robust feature of high latitude and deep ocean conditions. Persistently warm high latitude SSTs would mean that deep water formation would have remained sluggish. The largest cooling detected in the Weddell Sea occurs between the sampled windows of the late Miocene and the Pliocene. Using the TEX_{86} paleothermometer, we find SSTs cool to 2.8±1.1°C, 1σ, n=2) in the Pliocene, a drop of 7°C from the Miocene (**Figure 3**) similar to cooling during the Mid-Miocene Climate Transition (Shevenell et al., 2004) and late Miocene cooling >50 °N (Herbert et al., 2016). We hypothesize that this cooling of 7°C would have dramatically increased Antarctic Bottom Water formation in the Weddell Sea, and thus increased deep ocean ventilation and increased ocean overturning circulation. The Miocene to Pliocene cooling in the Weddell Sea is broadly commensurate with cooling detected in the deep ocean (**Figure 3c**) by clumped isotopes (Meckler et al., 2022), although much more data is needed to fill in the gaps in each record – both for clumped isotope deep ocean temperatures and Antarctic margin SSTs. More bottom temperature data are available based on the Mg/Ca of benthic foraminifera for the last 17 Ma (**Figure 3c**), with uncertainty shown associated with the changing Mg/Ca of seawater (Lear et al., 2015). Earlier Mg/Ca based estimates spanning the Cenozoic (Lear et al., 2000) and in the Miocene Southern Ocean (Shevenell et al., 2008) are cooler than the clumped estimates consistent with the expected

effects of changing seawater, nevertheless available seawater-corrected Mg/Ca based temperatures also find deep water cools during the Pliocene (Lear et al., 2015). Linking high latitude and deep water temperatures estimated by different methods has the potential to resolve some of these uncertainties about Cenozoic climate. Acquiring a more detailed oceanographic history of the Weddell Sea will only be possible through the recovery of more continuous sedimentary records through future drilling expeditions.

6. Conclusions

A multi-biomarker study of sedimentary drill cores captures signals of increasingly glacially-reworked sediments and tracks the cooling on land based on *br*GDGTs. In the Eocene, relatively warm summer (months above freezing) conditions occurred on the Antarctic Peninsula, Oligocene and even Miocene with MAF estimates of 11-12ºC. This demonstrates how the peninsula's warmth provided growing conditions for plants as refugia from the cooler conditions further south. However, *N. fusca* pollen decline in the Eocene, likely responding to a shortened growing season. In this study and in other applications where seasonality of climate may be changing, it may be generally helpful to consider the selective bias of the soil biomarker proxy, recording months above freezing. Here we find based on dual consideration of pollen and soil biomarkers, that as the climate cools, the winter frozen months lengthen, and the soil proxy is restricted to a short summer season, thus reconstructed MAF temperatures may appear to be relatively similar despite a possibly shorter time of thawed soil activity. Other indicators might be better sensors of winter cooling, e.g., sea ice indicators.

Ocean waters off the Antarctic Peninsula at 63ºS cooled from 12.5ºC in the Oligocene to 2.8ºC in the Pliocene based on BAYSPAR reconstructions. This evidence for ocean cooling near the Antarctic Peninsula adds to sparse regional data on the Southern Ocean. While the cooling broadly agrees with the expectation of global cooling and ice volume expansion reconstructed from the deep sea carbonates and the declining carbon dioxide levels in the atmosphere (**Figure 3**), there are some significant regional differences. We find warm ocean waters persist well into Neogene glaciation, confirming earlier tentative multi-proxy temperature data from Seymour Island (Douglas et al., 2014) and consistent with deep ocean temperature evidence (Lear et al., 2000, 2015; Meckler et al., 2022). The 7°C cooling of Weddell Sea temperatures, recorded by

771 TEX_{86} here, between the Miocene and the Pliocene marks the intensification of Antarctic Bottom
772 Water formation in the Weddell Sea, and thus increased deep ocean ventilation and ocean
773 overturning circulation.

774 As the iceberg delivery of pebbles in the Miocene and Pliocene attests, glacial advance was
775 accompanied by cooling on land on the Antarctic Peninsula, and there was distal transport of
776 terrestrial material from under the WAIS and EAIS, both of which were fully glaciated at that
777 time (Anderson et al., 2011; Naish et al., 2009). Icebergs calving into warm oceans yet persisting
778 to the tip of the Antarctic Peninsula, imply strong Weddell Sea circulation in iceberg alley as
779 previously noted (Carter et al., 2017). These new biomarker temperature estimates add to
780 knowledge of cooling of the eastern tip of the Antarctic Peninsula in "iceberg alley" critical to
781 this sensitive land-ocean boundary at the edge of the cryosphere. We find warm summers persist
782 even as winter temperatures dip, and that warm SSTs corroborate evidence from the deep sea.
783 These and hopefully more efforts to reconstruct Antarctic margins records are needed to
784 reconstruct past climate-cryosphere change and to support proxy-model comparison efforts to
785 develop mechanistic understanding of the Cenozoic evolution of Antarctic climate.

786 **Acknowledgements**

787 We declare no financial conflicts of interests for any author or their affiliations. This research
788 was funded by the U.S. National Science Foundation NSF-OPP-1908548 to SJF. This research
789 used samples and/or data collected by the RV/IB *Nathaniel B. Palmer* during SHALDRIL II,
790 supported by funding from the U.S. National Science Foundation. Samples were provided by
791 Oregon State University Marine and Geology Repository. Thanks to Miguel Rincon for
792 laboratory assistance in 2012 at USC, to Patrick Murphy for laboratory assistance with GDGT
793 analyses at the University of Arizona in 2021. Thanks to John Anderson for guidance on the
794 regional context, along with the constructive review input from the Associate Editor and an
795 anonymous reviewer, that improved this manuscript.

796 **Conflict of Interest**

797 The authors declare no financial conflicts of interests for any author or their affiliations.

798 **Open Research**

Data files are archived at the NOAA paleoclimatology database (Tibbett et al., 2022).

References

Anagnostou, E., John, E. H., Babila, T. L., Sexton, P. F., Ridgwell, A., Lunt, D. J., Pearson, P. N., Chalk, T. B., Pancost, R. D., & Foster, G. L. (2020). Proxy evidence for state-dependence of climate sensitivity in the Eocene greenhouse. *Nature Communications*, *11*(1), 4436. https://doi.org/10.1038/s41467-020-17887-x

Anagnostou, E., John, E. H., Edgar, K. M., Foster, G. L., Ridgwell, A., Inglis, G. N., Pancost, R. D., Lunt, D. J., & Pearson, P. N. (2016). Changing atmospheric CO2 concentration was the primary driver of early Cenozoic climate. *Nature*, *533*, 380.

Anderson, J. B. (2006). SHALDRIL II 2006 NBP0602A Cruise Report. *Rice University, Department of Earth Science, Houston, Texas*.

Anderson, J. B., Warny, S., Askin, R. A., Wellner, J. S., Bohaty, S. M., Kirshner, A. E., Livsey, D. N., Simms, A. R., Smith, T. R., Ehrmann, W., Lawver, L. A., Barbeau, D., Wise, S. W., Kulhanek, D. K., Weaver, F. M., & Majewski, W. (2011). Progressive Cenozoic cooling and the demise of Antarctica's last refugium. *Proceedings of the National Academy of Sciences*, *108*(28), 11356. https://doi.org/10.1073/pnas.1014885108

Anderson, J. B., & Wellner, J. S. (2012). SHALDRIL I and II: Drilling from the Research Vessel Icebreaker Nathaniel B. Palmer. *Oceanography*, *25*(3), 82.

Askin, R., & Raine, J. (2000). Oligocene and Early Miocene terrestrial palynology of the Cape Roberts Drillhole CRP-2/2A, Victoria Land Basin, Antarctica. *Terra Antartica*, *7*(4), 493–501.

Badger, M. P., Chalk, T. B., Foster, G. L., Bown, P. R., Gibbs, S. J., Sexton, P. F., Schmidt, D. N., Pälike, H., Mackensen, A., & Pancost, R. D. (2019). Insensitivity of alkenone carbon isotopes to atmospheric CO 2 at low to moderate CO 2 levels. *Climate of the Past*, *15*(2), 539–554.

822 Badger, M. P., Lear, C. H., Pancost, R. D., Foster, G. L., Bailey, T. R., Leng, M. J., & Abels, H. A.
823 (2013). CO2 drawdown following the middle Miocene expansion of the Antarctic Ice Sheet.
824 *Paleoceanography*, *28*(1), 42–53.
825 Bart, P. J., Egan, D., & Warny, S. A. (2005). Direct constraints on Antarctic Peninsula Ice Sheet
826 grounding events between 5.12 and 7.94 Ma. *Journal of Geophysical Research: Earth Surface*,
827 *110*(F4).
828 Bijl, P. K., Pross, J., Warnaar, J., Stickley, C. E., Huber, M., Guerstein, R., Houben, A. J. P., Sluijs, A.,
829 Visscher, H., & Brinkhuis, H. (2011). Environmental forcings of Paleogene Southern Ocean
830 dinoflagellate biogeography. *Paleoceanography*, *26*(1). https://doi.org/10.1029/2009PA001905
831 Bohaty, S. M., Kulhanek, D. K., Wise Jr, S. W., Jemison, K., Warny, S., & Sjunneskog, C. (2011). Age
832 assessment of Eocene–Pliocene drill cores recovered during the SHALDRIL II expedition,
833 Antarctic Peninsula. *Tectonic, Climatic, and Cryospheric Evolution of the Antarctic Peninsula*,
834 63–113.
835 Carter, A., Riley, T. R., Hillenbrand, C.-D., & Rittner, M. (2017). Widespread Antarctic glaciation during
836 the Late Eocene. *Earth and Planetary Science Letters*, *458*, 49–57.
837 https://doi.org/10.1016/j.epsl.2016.10.045
838 Coxall, H. K., & Pearson, P. N. (2007). The Eocene-Oligocene transition. *Deep Time Perspectives on*
839 *Climate Change: Marrying the Signal From Computer Models and Biological Proxies*, 351–387.
840 Coxall, H. K., Wilson, P. A., Palike, H., Lear, C. H., & Backman, J. (2005). Rapid stepwise onset of
841 Antarctic glaciation and deeper calcite compensation in the Pacific Ocean. *Nature*, *433*(7021),
842 53–57. https://doi.org/10.1038/nature03135
843 Davies, B. J., Hambrey, M. J., Smellie, J. L., Carrivick, J. L., & Glasser, N. F. (2012). Antarctic Peninsula
844 Ice Sheet evolution during the Cenozoic Era. *Quaternary Science Reviews*, *31*, 30–66.
845 https://doi.org/10.1016/j.quascirev.2011.10.012
846 De Jonge, C., Hopmans, E. C., Zell, C. I., Kim, J.-H., Schouten, S., & Sinninghe Damsté, J. S. (2014).
847 Occurrence and abundance of 6-methyl branched glycerol dialkyl glycerol tetraethers in soils:

Implications for palaeoclimate reconstruction. *Geochimica et Cosmochimica Acta*, *141*, 97–112. https://doi.org/10.1016/j.gca.2014.06.013

Dearing Crampton-Flood, E., Tierney, J. E., Peterse, F., Kirkels, F. M. S. A., & Sinninghe Damsté, J. S. (2020). BayMBT: A Bayesian calibration model for branched glycerol dialkyl glycerol tetraethers in soils and peats. *Geochimica et Cosmochimica Acta*, *268*, 142–159. https://doi.org/10.1016/j.gca.2019.09.043

Dingle, R. V., Marenssi, S. A., & Lavelle, M. (1998). High latitude Eocene climate deterioration: Evidence from the northern Antarctic Peninsula. *Journal of South American Earth Sciences*, *11*(6), 571–579. https://doi.org/10.1016/S0895-9811(98)00035-2

Douglas, P. M. J., Affek, H. P., Ivany, L. C., Houben, A. J. P., Sijp, W. P., Sluijs, A., Schouten, S., & Pagani, M. (2014). Pronounced zonal heterogeneity in Eocene southern high-latitude sea surface temperatures. *Proceedings of the National Academy of Sciences*, *111*(18), 6582. https://doi.org/10.1073/pnas.1321441111

Duffy, M., Tibbett, E. J., Smith, C., Warny, S., Feakins, S. J., Escarguel, G., Askin, R., Leventer, A., & Shevenell, A. E. (2022). Snapshots of pre-glacial paleoenvironmental conditions along the Sabrina Coast, East Antarctica: New palynological and biomarker evidence. *Geobios*, *70*, 1–16. https://doi.org/10.1016/j.geobios.2021.09.001

Duncan, B., McKay, R., Bendle, J., Naish, T., Inglis, G. N., Moossen, H., Levy, R., Ventura, G. T., Lewis, A., Chamberlain, B., & Walker, C. (2019). Lipid biomarker distributions in Oligocene and Miocene sediments from the Ross Sea region, Antarctica: Implications for use of biomarker proxies in glacially-influenced settings. *Palaeogeography, Palaeoclimatology, Palaeoecology*, *516*, 71–89. https://doi.org/10.1016/j.palaeo.2018.11.028

Edwards, L. E., Mudie, P. J., & de Vernal, A. (1991). Pliocene paleoclimatic reconstruction using dinoflagellate cysts: Comparison of methods. *Quaternary Science Reviews*, *10*(2), 259–274. https://doi.org/10.1016/0277-3791(91)90024-O

873 Evangelinos, D., Escutia, C., Etourneau, J., Hoem, F., Bijl, P., Boterblom, W., van de Flierdt, T., Valero,
874 L., Flores, J.-A., Rodriguez-Tovar, F. J., Jimenez-Espejo, F. J., Salabarnada, A., & López-Quirós,
875 A. (2020). Late Oligocene-Miocene proto-Antarctic Circumpolar Current dynamics off the
876 Wilkes Land margin, East Antarctica. *Global and Planetary Change*, *191*, 103221.
877 https://doi.org/10.1016/j.gloplacha.2020.103221
878 Feakins, S. J., Warny, S., & DeConto, R. M. (2014). Snapshot of cooling and drying before onset of
879 Antarctic Glaciation. *Earth and Planetary Science Letters*, *404*, 154–166.
880 https://doi.org/10.1016/j.epsl.2014.07.032
881 Feakins, S. J., Warny, S., & Lee, J.-E. (2012). Hydrologic cycling over Antarctica during the middle
882 Miocene warming. *Nature Geoscience*, *5*(8), 557–560. https://doi.org/10.1038/NGEO1498
883 Foster, G. L., Lear, C. H., & Rae, J. W. (2012). The evolution of pCO2, ice volume and climate during
884 the middle Miocene. *Earth and Planetary Science Letters*, *341*, 243–254.
885 Francelino, M. R., Schaefer, C., Skansi, M. de L. M., Colwell, S., Bromwich, D. H., Jones, P., King, J. C.,
886 Lazzara, M. A., Renwick, J., Solomon, S., Brunet, M., & Cerveny, R. S. (2021). WMO
887 Evaluation of Two Extreme High Temperatures Occurring in February 2020 for the Antarctic
888 Peninsula Region. *Bulletin of the American Meteorological Society*, *102*(11), E2053–E2061.
889 https://doi.org/10.1175/BAMS-D-21-0040.1
890 Francis, J., Ashworth, A., Cantrill, D., Crame, J., Howe, J., Stephens, R., Tosolini, A., & Thorn, V.
891 (2008). 100 million years of Antarctic climate evolution: Evidence from fossil plants. *Antarctica:*
892 *A Keystone in a Changing World*, 19–28.
893 Francis, J. E., Marenssi, S., Levy, R., Hambrey, M., Thorn, V. C., Mohr, B., Brinkhuis, H., Warnaar, J.,
894 Zachos, J., Bohaty, S., & DeConto, R. (2008). Chapter 8 From Greenhouse to Icehouse – The
895 Eocene/Oligocene in Antarctica. In F. Florindo & M. Siegert (Eds.), *Developments in Earth and*
896 *Environmental Sciences* (Vol. 8, pp. 309–368). Elsevier. https://doi.org/10.1016/S1571-
897 9197(08)00008-6

898 Fretwell, P., Pritchard, H. D., Vaughan, D. G., Bamber, J. L., Barrand, N. E., Bell, R., Bianchi, C.,
899 Bingham, R. G., Blankenship, D. D., Casassa, G., Catania, G., Callens, D., Conway, H., Cook, A.
900 J., Corr, H. F. J., Damaske, D., Damm, V., Ferraccioli, F., Forsberg, R., … Zirizzotti, A. (2013).
901 Bedmap2: Improved ice bed, surface and thickness datasets for Antarctica. *Cryosphere*, *7*(1),
902 375–393. https://doi.org/10.5194/tc-7-375-2013
903 Gohl, K., Uenzelmann-Neben, G., Gille-Petzoldt, J., Hillenbrand, C., Klages, J. P., Bohaty, S. M.,
904 Passchier, S., Frederichs, T., Wellner, J. S., & Lamb, R. (2021). Evidence for a highly dynamic
905 West Antarctic Ice Sheet during the Pliocene. *Geophysical Research Letters*, *48*(14),
906 e2021GL093103.
907 Goldner, A., Herold, N., & Huber, M. (2014). Antarctic glaciation caused ocean circulation changes at the
908 Eocene–Oligocene transition. *Nature*, *511*(7511), 574–577. https://doi.org/10.1038/nature13597
909 Greene, C. A., Gwyther, D. E., & Blankenship, D. D. (2017). Antarctic mapping tools for MATLAB.
910 *Computers & Geosciences*, *104*, 151–157.
911 Greenop, R., Foster, G. L., Wilson, P. A., & Lear, C. H. (2014). Middle Miocene climate instability
912 associated with high-amplitude CO2 variability. *Paleoceanography*, *29*(9), 845–853.
913 Greenop, R., Sosdian, S. M., Henehan, M. J., Wilson, P. A., Lear, C. H., & Foster, G. L. (2019). Orbital
914 forcing, ice volume, and CO2 across the Oligocene-Miocene transition. *Paleoceanography and*
915 *Paleoclimatology*, *34*(3), 316–328.
916 Griener, K. W., Nelson, D. M., & Warny, S. (2013). Declining moisture availability on the Antarctic
917 Peninsula during the Late Eocene. *Palaeogeography, Palaeoclimatology, Palaeoecology*, *383*,
918 72–78.
919 Hartman, J. D., Sangiorgi, F., Salabarnada, A., Peterse, F., Houben, A. J. P., Schouten, S., Brinkhuis, H.,
920 Escutia, C., & Bijl, P. K. (2018). Paleoceanography and ice sheet variability offshore Wilkes
921 Land, Antarctica – Part 3: Insights from Oligocene–Miocene TEX_{86}-based sea surface
922 temperature reconstructions. *Climate of the Past*, *14*(9), 1275–1297. https://doi.org/10.5194/cp-
923 14-1275-2018

924 Henehan, M. J., Edgar, K. M., Foster, G. L., Penman, D. E., Hull, P. M., Greenop, R., Anagnostou, E., &
925 Pearson, P. N. (2020). Revisiting the Middle Eocene Climatic Optimum “Carbon Cycle
926 Conundrum” with new estimates of atmospheric pCO2 from boron isotopes. *Paleoceanography*
927 *and Paleoclimatology*, *35*(6), e2019PA003713.
928 Herbert, T. D., Lawrence, K. T., Tzanova, A., Peterson, L. C., Caballero-Gill, R., & Kelly, C. S. (2016).
929 Late Miocene global cooling and the rise of modern ecosystems. *Nature Geoscience*, *9*(11), 843–
930 847. https://doi.org/10.1038/ngeo2813
931 Hopmans, E. C., Schouten, S., & Sinninghe Damsté, J. S. (2016). The effect of improved chromatography
932 on GDGT-based palaeoproxies. *Organic Geochemistry*, *93*, 1–6.
933 https://doi.org/10.1016/j.orggeochem.2015.12.006
934 Hopmans, E. C., Weijers, J. W. H., Schefuß, E., Herfort, L., Sinninghe Damsté, J. S., & Schouten, S.
935 (2004). A novel proxy for terrestrial organic matter in sediments based on branched and
936 isoprenoid tetraether lipids. *Earth and Planetary Science Letters*, *224*(1), 107–116.
937 https://doi.org/10.1016/j.epsl.2004.05.012
938 Houben, A. J. P., Bijl, P. K., Guerstein, G. R., Sluijs, A., & Brinkhuis, H. (2011). Malvinia escutiana, a
939 new biostratigraphically important Oligocene dinoflagellate cyst from the Southern Ocean.
940 *Review of Palaeobotany and Palynology*, *165*(3), 175–182.
941 https://doi.org/10.1016/j.revpalbo.2011.03.002
942 Houben, A. J. P., Bijl, P. K., Sluijs, A., Schouten, S., & Brinkhuis, H. (2019, May 1). *Late Eocene*
943 *Southern Ocean Cooling and Invigoration of Circulation Preconditioned Antarctica for Full-*
944 *Scale Glaciation*. Geochemistry, Geophysics, Geosystems.
945 https://doi.org/10.1029/2019GC008182
946 Huguet, C., Hopmans, E. C., Febo-Ayala, W., Thompson, D. H., Sinninghe Damsté, J. S., & Schouten, S.
947 (2006). An improved method to determine the absolute abundance of glycerol dibiphytanyl
948 glycerol tetraether lipids. *Organic Geochemistry*, *37*(9), 1036–1041.
949 https://doi.org/10.1016/j.orggeochem.2006.05.008

Hunt, R. J., & Poole, I. (2003). *Paleogene West Antarctic climate and vegetation history in light of new data from King George Island*.

Inglis, G. N., Naafs, B. D. A., Zheng, Y., McClymont, E. L., Evershed, R. P., & Pancost, R. D. (2018). Distributions of geohopanoids in peat: Implications for the use of hopanoid-based proxies in natural archives. *Geochimica et Cosmochimica Acta*, *224*, 249–261. https://doi.org/10.1016/j.gca.2017.12.029

Inglis, G. N., Toney, J. L., Zhu, J., Poulsen, C. J., Röhl, U., Jamieson, S. S. R., Pross, J., Cramwinckel, M. J., Krishnan, S., Pagani, M., Bijl, P. K., & Bendle, J. (2022). Enhanced Terrestrial Carbon Export From East Antarctica During the Early Eocene. *Paleoceanography and Paleoclimatology*, *37*(2), e2021PA004348. https://doi.org/10.1029/2021PA004348

Judd, E. J., Ivany, L. C., DeConto, R. M., Halberstadt, A. R. W., Miklus, N. M., Junium, C. K., & Uveges, B. T. (2019). Seasonally Resolved Proxy Data From the Antarctic Peninsula Support a Heterogeneous Middle Eocene Southern Ocean. *Paleoceanography and Paleoclimatology*, *34*(5), 787–799. https://doi.org/10.1029/2019PA003581

Kirshner, A. E., & Anderson, J. B. (2011). *Cenozoic glacial history of the northern Antarctic Peninsula: A micromorphological investigation of quartz sand grains*.

Kvenvolden, K., D. Hostettler, F., B. Rapp, J., & Frank, T. (1991). 23. Aliphatic hydrocarbons in sediments from Prydz Bay, Antarctica. *Proceedings of Ocean Drilling Program*, *Part B*(119), 417–423.

Lauretano, V., Kennedy-Asser, A. T., Korasidis, V. A., Wallace, M. W., Valdes, P. J., Lunt, D. J., Pancost, R. D., & Naafs, B. D. A. (2021). Eocene to Oligocene terrestrial Southern Hemisphere cooling caused by declining pCO2. *Nature Geoscience*, *14*(9), 659–664. https://doi.org/10.1038/s41561-021-00788-z

Lear, C. H., Coxall, H. K., Foster, G. L., Lunt, D. J., Mawbey, E. M., Rosenthal, Y., Sosdian, S. M., Thomas, E., & Wilson, P. A. (2015). Neogene ice volume and ocean temperatures: Insights from

975 infaunal foraminiferal Mg/Ca paleothermometry. *Paleoceanography*, *30*(11), 1437–1454.
976 https://doi.org/10.1002/2015PA002833
977 Lear, C. H., Elderfield, H., & Wilson, P. A. (2000). Cenozoic Deep-Sea Temperatures and Global Ice
978 Volumes from Mg/Ca in Benthic Foraminiferal Calcite. *Science*, *287*(5451), 269–272.
979 https://doi.org/10.1126/science.287.5451.269
980 Leutert, T. J., Auderset, A., Martínez-García, A., Modestou, S., & Meckler, A. N. (2020). Coupled
981 Southern Ocean cooling and Antarctic ice sheet expansion during the middle Miocene. *Nature*
982 *Geoscience*, *13*(9), 634–639. https://doi.org/10.1038/s41561-020-0623-0
983 Levy, R. H., Meyers, S., Naish, T. R., Golledge, N. R., McKay, R. M., Crampton, J. S., DeConto, R., De
984 Santis, L., Florindo, F., & Gasson, E. G. (2019). Antarctic ice-sheet sensitivity to obliquity
985 forcing enhanced through ocean connections. *Nature Geoscience*, *12*(2), 132–137.
986 Levy, R., Harwood, D., Florindo, F., Sangiorgi, F., Tripati, R., Von Eynatten, H., Gasson, E., Kuhn, G.,
987 Tripati, A., & DeConto, R. (2016). Antarctic ice sheet sensitivity to atmospheric CO2 variations
988 in the early to mid-Miocene. *Proceedings of the National Academy of Sciences*, *113*(13), 3453–
989 3458.
990 Lewis, A. R., Marchant, D. R., Ashworth, A. C., Hedenäs, L., Hemming, S. R., Johnson, J. V., Leng, M.
991 J., Machlus, M. L., Newton, A. E., Raine, J. I., Willenbring, J. K., Williams, M., & Wolfe, A. P.
992 (2008). Mid-Miocene cooling and the extinction of tundra in continental Antarctica. *Proceedings*
993 *of the National Academy of Sciences*, *105*(31), 10676. https://doi.org/10.1073/pnas.0802501105
994 Liu, Z., Pagani, M., Zinniker, D., DeConto, R., Huber, M., Brinkhuis, H., Shah, S. R., Leckie, R. M., &
995 Pearson, A. (2009). Global Cooling During the Eocene-Oligocene Climate Transition. *Science*,
996 *323*(5918), 1187. https://doi.org/10.1126/science.1166368
997 Macphail, M. K., & Truswell, E. M. (2004). Palynology of Neogene slope and rise deposits from ODP
998 Sites 1165 and 1167, East Antarctica. *Proceedings of the Ocean Drilling Program. Scientific*
999 *Results*, *188*, 1–20.

1000 Marenssi, S. A., Casadío, S., & Santillana, S. N. (2010). Record of Late Miocene glacial deposits on Isla
1001 Marambio (Seymour Island), Antarctic Peninsula. *Antarctic Science*, *22*(2), 193–198. Cambridge
1002 Core. https://doi.org/10.1017/S0954102009990629
1003 Martínez-Sosa, P., Tierney, J. E., Stefanescu, I. C., Dearing Crampton-Flood, E., Shuman, B. N., &
1004 Routson, C. (2021). A global Bayesian temperature calibration for lacustrine brGDGTs.
1005 *Geochimica et Cosmochimica Acta*, *305*, 87–105. https://doi.org/10.1016/j.gca.2021.04.038
1006 McKay, R. M., Escutia, C., Santis, L. D., Donda, F., Duncan, B., Gohl, K., Gulick, S., Hernández-Molina,
1007 J., Hillenbrand, C.-D., Hochmuth, K., Kim, S., Kuhn, G., Larter, R., Leitchenkov, G., Levy, R.
1008 H., Naish, T. R., O'Brien, P., Pérez, L. F., Shevenell, A. E., & Williams, T. (2022). Chapter 3—
1009 Cenozoic history of Antarctic glaciation and climate from onshore and offshore studies. In F.
1010 Florindo, M. Siegert, L. D. Santis, & T. Naish (Eds.), *Antarctic Climate Evolution (Second*
1011 *Edition)* (Second Edition, pp. 41–164). Elsevier. https://doi.org/10.1016/B978-0-12-819109-
1012 5.00008-6
1013 McKay, R., Naish, T., Carter, L., Riesselman, C., Dunbar, R., Sjunneskog, C., Winter, D., Sangiorgi, F.,
1014 Warren, C., Pagani, M., Schouten, S., Willmott, V., Levy, R., DeConto, R., & Powell, R. D.
1015 (2012). Antarctic and Southern Ocean influences on Late Pliocene global cooling. *Proceedings of*
1016 *the National Academy of Sciences*, *109*(17), 6423. https://doi.org/10.1073/pnas.1112248109
1017 Meckler A. N., Sexton P. F., Piasecki A. M., Leutert T. J., Marquardt J., Ziegler M., Agterhuis T.,
1018 Lourens L. J., Rae J. W. B., Barnet J., Tripati A., & Bernasconi S. M. (2022). Cenozoic evolution
1019 of deep ocean temperature from clumped isotope thermometry. *Science*, *377*(6601), 86–90.
1020 https://doi.org/10.1126/science.abk0604
1021 Mohr, B. (1990). Eocene and Oligocene Sporomorphs and Dinoflagellate Cysts from Leg 113 Drill
1022 Sites|Weddell Sea|Antarctica. *Proc., Scientific Results, ODP, Leg 113, Weddell Sea, Antarctica*,
1023 *120*. https://doi.org/10.2973/odp.proc.sr.113.140.1990
1024 Mudie, P. J. (1992). Circum-Arctic Quaternary and Neogene marine palynofloras: Paleoecology and
1025 statistical analysis. *Neogene and Quaternary Dinoflagellate Cysts and Acritarchs*, *10*, 347–390.

1026 Naish, T., Powell, R., Levy, R., Wilson, G., Scherer, R., Talarico, F., Krissek, L., Niessen, F., Pompilio,
1027 M., Wilson, T., Carter, L., DeConto, R., Huybers, P., McKay, R., Pollard, D., Ross, J., Winter,
1028 D., Barrett, P., Browne, G., … Williams, T. (2009). Obliquity-paced Pliocene West Antarctic ice
1029 sheet oscillations. *Nature*, *458*(7236), 322–328. https://doi.org/10.1038/nature07867
1030 O'Brien, C. L., Huber, M., Thomas, E., Pagani, M., Super, J. R., Elder, L. E., & Hull, P. M. (2020). The
1031 enigma of Oligocene climate and global surface temperature evolution. *Proceedings of the*
1032 *National Academy of Sciences*, *117*(41), 25302. https://doi.org/10.1073/pnas.2003914117
1033 Pagani, M., Huber, M., Liu, Z., Bohaty, S. M., Henderiks, J., Sijp, W., Krishnan, S., & DeConto, R. M.
1034 (2011). The Role of Carbon Dioxide During the Onset of Antarctic Glaciation. *Science*,
1035 *334*(6060), 1261. https://doi.org/10.1126/science.1203909
1036 Pagani, M., Liu, Z., LaRiviere, J., & Ravelo, A. C. (2010). High Earth-system climate sensitivity
1037 determined from Pliocene carbon dioxide concentrations. *Nature Geoscience*, *3*(1), 27–30.
1038 Pagani, M., Zachos, J. C., Freeman, K. H., Tipple, B., & Bohaty, S. (2005). Marked Decline in
1039 Atmospheric Carbon Dioxide Concentrations During the Paleogene. *Science*, *309*(5734), 600.
1040 https://doi.org/10.1126/science.1110063
1041 Passchier, S., Bohaty, S. M., Jimenez-Espejo, F. J., Pross, J., Roehl, U., van de Flierdt, T., Escutia, C., &
1042 Brinkhuis, H. (2013). Early Eocene to middle Miocene cooling and aridification of East
1043 Antarctica. *Geochemistry Geophysics Geosystems*, *14*(5), 1399–1410.
1044 https://doi.org/10.1002/ggge.20106
1045 Passchier, S., Ciarletta, D. J., Miriagos, T. E., Bijl, P. K., & Bohaty, S. M. (2017). An Antarctic
1046 stratigraphic record of stepwise ice growth through the Eocene-Oligocene transition. *Geological*
1047 *Society of America Bulletin*, *129*(3–4), 318–330. https://doi.org/10.1130/B31482.1
1048 Pearson, P. N., Foster, G. L., & Wade, B. S. (2009). Atmospheric carbon dioxide through the Eocene–
1049 Oligocene climate transition. *Nature*, *461*(7267), 1110–1113. https://doi.org/10.1038/nature08447

Petersen, S. V., & Schrag, D. P. (2015). Antarctic ice growth before and after the Eocene-Oligocene transition: New estimates from clumped isotope paleothermometry: Antarctic ice growth at the E/O transition. *Paleoceanography*, *30*(10), 1305–1317. https://doi.org/10.1002/2014PA002769

Plancq, J., Mattioli, E., Pittet, B., Simon, L., & Grossi, V. (2014). Productivity and sea-surface temperature changes recorded during the late Eocene–early Oligocene at DSDP Site 511 (South Atlantic). *Palaeogeography, Palaeoclimatology, Palaeoecology*, *407*, 34–44. https://doi.org/10.1016/j.palaeo.2014.04.016

Poole, I., Cantrill, D., & Utescher, T. (2005). A multi-proxy approach to determine Antarctic terrestrial palaeoclimate during the Late Cretaceous and Early Tertiary. *Palaeogeography, Palaeoclimatology, Palaeoecology*, *222*(1), 95–121. https://doi.org/10.1016/j.palaeo.2005.03.011

Pound, M. J., & Salzmann, U. (2017). Heterogeneity in global vegetation and terrestrial climate change during the late Eocene to early Oligocene transition. *Scientific Reports*, *7*, 43386. https://doi.org/10.1038/srep43386

Prebble, J. G., Raine, J. I., Barrett, P. J., & Hannah, M. J. (2006). Vegetation and climate from two Oligocene glacioeustatic sedimentary cycles (31 and 24 Ma) cored by the Cape Roberts Project, Victoria Land Basin, Antarctica. *Antarctic Climate Evolution: Geological Records from the Margin and Modelling*, *231*(1), 41–57. https://doi.org/10.1016/j.palaeo.2005.07.025

Rae, J. W. B., Zhang, Y. G., Liu, X., Foster, G. L., Stoll, H. M., & Whiteford, R. D. M. (2021). Atmospheric CO2 over the Past 66 Million Years from Marine Archives. *Annual Review of Earth and Planetary Sciences*, *49*(1), 609–641. https://doi.org/10.1146/annurev-earth-082420-063026

Raine, J. (1998). Terrestrial palynomorphs from Cape Roberts Project drillhole CRP-1, Ross Sea, Antarctica. *Terra Antartica*, *5*(3), 539–548.

Rose, K. C., Ferraccioli, F., Jamieson, S. S. R., Bell, R. E., Corr, H., Creyts, T. T., Braaten, D., Jordan, T. A., Fretwell, P. T., & Damaske, D. (2013). Early East Antarctic Ice Sheet growth recorded in the landscape of the Gamburtsev Subglacial Mountains. *Earth and Planetary Science Letters*, *375*, 1–12. https://doi.org/10.1016/j.epsl.2013.03.053

1076 Salzmann, U., Riding, J. B., Nelson, A. E., & Smellie, J. L. (2011). How likely was a green Antarctic
1077 Peninsula during warm Pliocene interglacials? A critical reassessment based on new palynofloras
1078 from James Ross Island. *Special Issue: Climate and Seasonality in a Pliocene Warm World*,
1079 *309*(1), 73–82. https://doi.org/10.1016/j.palaeo.2011.01.028
1080 Sangiorgi, F., Bijl, P. K., Passchier, S., Salzmann, U., Schouten, S., McKay, R., Cody, R. D., Pross, J.,
1081 van de Flierdt, T., Bohaty, S. M., Levy, R., Williams, T., Escutia, C., & Brinkhuis, H. (2018).
1082 Southern Ocean warming and Wilkes Land ice sheet retreat during the mid-Miocene. *Nature*
1083 *Communications*, *9*(1), 317. https://doi.org/10.1038/s41467-017-02609-7
1084 Schouten, S., Huguet, C., Hopmans, E. C., Kienhuis, M. V. M., & Sinninghe Damsté, J. S. (2007).
1085 Analytical Methodology for TEX86 Paleothermometry by High-Performance Liquid
1086 Chromatography/Atmospheric Pressure Chemical Ionization-Mass Spectrometry. *Analytical*
1087 *Chemistry*, *79*(7), 2940–2944. https://doi.org/10.1021/ac062339v
1088 Sessions, A. L., Zhang, L., Welander, P. V., Doughty, D., Summons, R. E., & Newman, D. K. (2013).
1089 Identification and quantification of polyfunctionalized hopanoids by high temperature gas
1090 chromatography-mass spectrometry. *Organic Geochemistry*, *56*, 120–130. PubMed.
1091 https://doi.org/10.1016/j.orggeochem.2012.12.009
1092 Shevenell, A. E., Kennett, J. P., & Lea, D. W. (2004). Middle Miocene southern ocean cooling and
1093 Antarctic cryosphere expansion. *Science*, *305*(5691), 1766–1770.
1094 Shevenell, A. E., Kennett, J. P., & Lea, D. W. (2008). Middle Miocene ice sheet dynamics, deep-sea
1095 temperatures, and carbon cycling: A Southern Ocean perspective. *Geochemistry, Geophysics,*
1096 *Geosystems*, *9*(2). https://doi.org/10.1029/2007GC001736
1097 Sinninghe Damsté, J. S. (2016). Spatial heterogeneity of sources of branched tetraethers in shelf systems:
1098 The geochemistry of tetraethers in the Berau River delta (Kalimantan, Indonesia). *Geochimica et*
1099 *Cosmochimica Acta*, *186*, 13–31. https://doi.org/10.1016/j.gca.2016.04.033

Smith, R. T., & Anderson, J. B. (2010). Ice-sheet evolution in James Ross Basin, Weddell Sea margin of the Antarctic Peninsula: The seismic stratigraphic record. *GSA Bulletin*, *122*(5–6), 830–842. https://doi.org/10.1130/B26486.1

Sosdian, S. M., Greenop, R., Hain, M., Foster, G. L., Pearson, P. N., & Lear, C. H. (2018). Constraining the evolution of Neogene ocean carbonate chemistry using the boron isotope pH proxy. *Earth and Planetary Science Letters*, *498*, 362–376.

Stocchi, P., Escutia, C., Houben, A. J. P., Vermeersen, B. L. A., Bijl, P. K., Brinkhuis, H., DeConto, R. M., Galeotti, S., Passchier, S., Pollard, D., Brinkhuis, H., Escutia, C., Klaus, A., Fehr, A., Williams, T., Bendle, J. A. P., Bijl, P. K., Bohaty, S. M., Carr, S. A., … Yamane, M. (2013). Relative sea-level rise around East Antarctica during Oligocene glaciation. *Nature Geoscience*, *6*(5), 380–384. https://doi.org/10.1038/ngeo1783

Thompson, N., Salzmann, U., López-Quirós, A., Bijl, P. K., Hoem, F. S., Etourneau, J., Sicre, M.-A., Roignant, S., Hocking, E., Amoo, M., & Escutia, C. (2022). Vegetation change across the Drake Passage region linked to late Eocene cooling and glacial disturbance after the Eocene–Oligocene transition. *Climate of the Past*, *18*(2), 209–232. https://doi.org/10.5194/cp-18-209-2022

Tibbett, E. J., Scher, H. D., Warny, S., Tierney, J. E., Passchier, S., & Feakins, S. J. (2021). Late Eocene Record of Hydrology and Temperature From Prydz Bay, East Antarctica. *Paleoceanography and Paleoclimatology*, *36*(4), e2020PA004204. https://doi.org/10.1029/2020PA004204

Tibbett, E. J., Warny, S., Tierney, J. E., Wellner, J. S., & Feakins, S. J. (2022). SHALDRIL Antarctic Peninsula, biomarkers, 37-3 million years [Dataset]. *NOAA Paleoclimate Database*. https://www.ncdc.noaa.gov/paleo/study/35613

Tierney, J. E., & Tingley, M. P. (2014). A Bayesian, spatially-varying calibration model for the TEX86 proxy. *Geochimica et Cosmochimica Acta*, *127*, 83–106. https://doi.org/10.1016/j.gca.2013.11.026

Truswell, E. M., & Macphail, M. K. (2009). Polar forests on the edge of extinction: What does the fossil spore and pollen evidence from East Antarctica say? *Australian Systematic Botany*, *22*(2), 57–106. https://doi.org/10.1071/SB08046

Turner, J., Marshall, G. J., Clem, K., Colwell, S., Phillips, T., & Lu, H. (2020). Antarctic temperature variability and change from station data. *International Journal of Climatology*, *40*(6), 2986–3007. https://doi.org/10.1002/joc.6378

Uemura, H., & Ishiwatari, R. (1995). Identification of unusual 17β(H)-moret-22(29)-ene in lake sediments. *Organic Geochemistry*, *23*(7), 675–680. https://doi.org/10.1016/0146-6380(95)00036-E

Warny, S., & Askin, R. (2011a). Last remnants of Cenozoic vegetation and organic-walled phytoplankton in the Antarctic Peninsula's icehouse world. In *Tectonic, climatic, and cryospheric evolution of the Antarctic peninsula* (Vol. 63, pp. 167–192). American Geophysical Union Washington, DC.

Warny, S., & Askin, R. (2011b). Vegetation and Organic-Walled Phytoplankton at the End of the Antarctic Greenhouse World: Latest Eocene Cooling Events. In *Tectonic, Climatic, and Cryospheric Evolution of the Antarctic Peninsula* (pp. 193–210). American Geophysical Union (AGU). https://doi.org/10.1029/2010SP000965

Warny, S., Askin, R. A., Hannah, M. J., Mohr, B. A. R., Raine, J. I., Harwood, D. M., Florindo, F., & the SMS Science Team. (2009). Palynomorphs from a sediment core reveal a sudden remarkably warm Antarctica during the middle Miocene. *Geology*, *37*(10), 955–958. https://doi.org/10.1130/G30139A.1

Warny, S., Kymes, C. M., Askin, R., Krajewski, K. P., & Tatur, A. (2019). Terrestrial and marine floral response to latest Eocene and Oligocene events on the Antarctic Peninsula. *Palynology*, *43*(1), 4–21. https://doi.org/10.1080/01916122.2017.1418444

Warny, S., Wrenn, J. H., Bart, P. J., & Askin, R. (2006). Palynology of the NBP03–01A transect in the Northern Basin, Western Ross Sea, Antarctica: A late Pliocene record. *Palynology*, *30*(1), 151–182. https://doi.org/10.1080/01916122.2006.9989624

Weijers, J. W. H., Schouten, S., Spaargaren, O. C., & Sinninghe Damsté, J. S. (2006). Occurrence and distribution of tetraether membrane lipids in soils: Implications for the use of the TEX86 proxy and the BIT index. *Advances in Organic Geochemistry 2005*, *37*(12), 1680–1693. https://doi.org/10.1016/j.orggeochem.2006.07.018

Wellner, J. S., Anderson, J. B., Ehrmann, W., Weaver, F. M., Kirshner, A., Livsey, D., & Simms, A. R. (2011). History of an Evolving Ice Sheet as Recorded in SHALDRIL Cores from the Northwestern Weddell Sea, Antarctica. In *Tectonic, Climatic, and Cryospheric Evolution of the Antarctic Peninsula* (pp. 131–151). American Geophysical Union (AGU). https://doi.org/10.1029/2010SP001047

Westerhold, T., Marwan, N., Drury, A. J., Liebrand, D., Agnini, C., Anagnostou, E., Barnet, J. S. K., Bohaty, S. M., Vleeschouwer, D. D., Florindo, F., Frederichs, T., Hodell, D. A., Holbourn, A. E., Kroon, D., Lauretano, V., Littler, K., Lourens, L. J., Lyle, M., Pälike, H., … Zachos, J. C. (2020). An astronomically dated record of Earth’s climate and its predictability over the last 66 million years. *Science*, *369*(6509), 1383–1387. https://doi.org/10.1126/science.aba6853

Zhang, Y. G., Pagani, M., Liu, Z., Bohaty, S. M., & DeConto, R. (2013). A 40-million-year history of atmospheric CO2. *Philosophical Transactions of the Royal Society A: Mathematical, Physical and Engineering Sciences*, *371*(2001), 20130096. https://doi.org/10.1098/rsta.2013.0096

Zhang, Y. G., Pagani, M., & Wang, Z. (2016). Ring Index: A new strategy to evaluate the integrity of TEX86 paleothermometry. *Paleoceanography*, *31*(2), 220–232. https://doi.org/10.1002/2015PA002848

Zhang, Y. G., Zhang, C. L., Liu, X.-L., Li, L., Hinrichs, K.-U., & Noakes, J. E. (2011). Methane Index: A tetraether archaeal lipid biomarker indicator for detecting the instability of marine gas hydrates. *Earth and Planetary Science Letters*, *307*(3), 525–534. https://doi.org/10.1016/j.epsl.2011.05.031

Supplemental References

Hochmuth, K., Gohl, K., Leitchenkov, G., Sauermilch, I., Whittaker, J.M., Uenzelmann-Neben, G., Davy, B. and De Santis, L. (2020) The Evolving Paleobathymetry of the Circum-Antarctic Southern Ocean Since 34 Ma: A Key to Understanding Past Cryosphere-Ocean Developments. Geochemistry, Geophysics, Geosystems 21, e2020GC009122. https://doi.org/10.1029/2020GC009122.

Figure Captions

Figure 1: Map of the present day Antarctic Peninsula bed elevation (Fretwell et al., 2013; Greene et al., 2017), showing SHALDRIL II drilling locations (white stars). Red arrows illustrate the Weddell Gyre circulation. Inset map shows location of the Antarctic Peninsula on Antarctica.

Figure 2. Data from SHALDRIL II a) summarizing age control (Bohaty et al., 2011), b) lithology, c) pebble count, d) the proportion of *Nothofagus fusca* and reworked pollen (Anderson et al., 2011), and e-k) new biomarker data (this study). Biomarker results include: e) the hopane index, f) *n*-alkane CPI, g) BIT index, h) ACL and i) concentrations of both the *n*-alkanoic acid and *n*-alkane compound classes, j) *br*- and *iso*GDGT concentrations and k) the MBT'_{5Me}-based temperature reconstructions using two available soil calibrations to estimate MAAT (Dearing Crampton Flood et al., 2020) and MAF (Martínez-Sosa et al., 2021), as well as the TEX_{86}-based BAYSPAR estimates of SST available for a subset of the samples. The declining alkane CPI, declining hopane ββ/(αβ+βα+ββ) index, and increasing reworked pollen all show more reworking up section in parallel to cooling. Concentration data for the *n*-alkanoic acids from the Eocene section is limited due to sample use for isotopic analyses (Feakins et al., 2014).

Figure 3. Compiled Cenozoic temperature records from Antarctica and the surrounding Southern Ocean including SHALDRIL II (yellow squares, this study). a) Map depicting proxy site locations, symbol fill colors in a-c correspond to different ocean sectors Indian Ocean (orange), Western Pacific (black), Ross Sea (blue), Weddell Sea (brown), and differentiates land (white outline), and ocean temperature proxies (black outline). b) Surface air temperature (Douglas et al., 2014; Feakins et al., 2012; Passchier et al., 2013, 2017; Thompson et al., 2022; Tibbett et al., 2021). Pollen (green) derives from Antarctic Peninsula (Francis et al., 2008), Ross Sea (Askin & Raine, 2000; Francis et al., 2008; Lewis et al., 2008; Prebble et al., 2006; Raine, 1998; Warny et

al., 2009), and Indian Ocean sector (Macphail & Truswell, 2004; Truswell & Macphail, 2009). c) Sea surface temperature (Douglas et al., 2014; Evangelinos et al., 2020; Hartman et al., 2018; Houben et al., 2019; Lauretano et al., 2021; Leutert et al., 2020; Levy et al., 2016; Liu et al., 2009; McKay et al., 2012; Petersen & Schrag, 2015; Plancq et al., 2014; Shevenell et al., 2004) and deep water temperature (DWT) based on Mg/Ca (Lear et al., 2015) and clumped isotopes (Meckler et al., 2022). d) Comparison global data $\delta^{18}O_{benthic}$ record splice (Westerhold et al., 2020) and pCO_2 compilation (Rae et al., 2021).

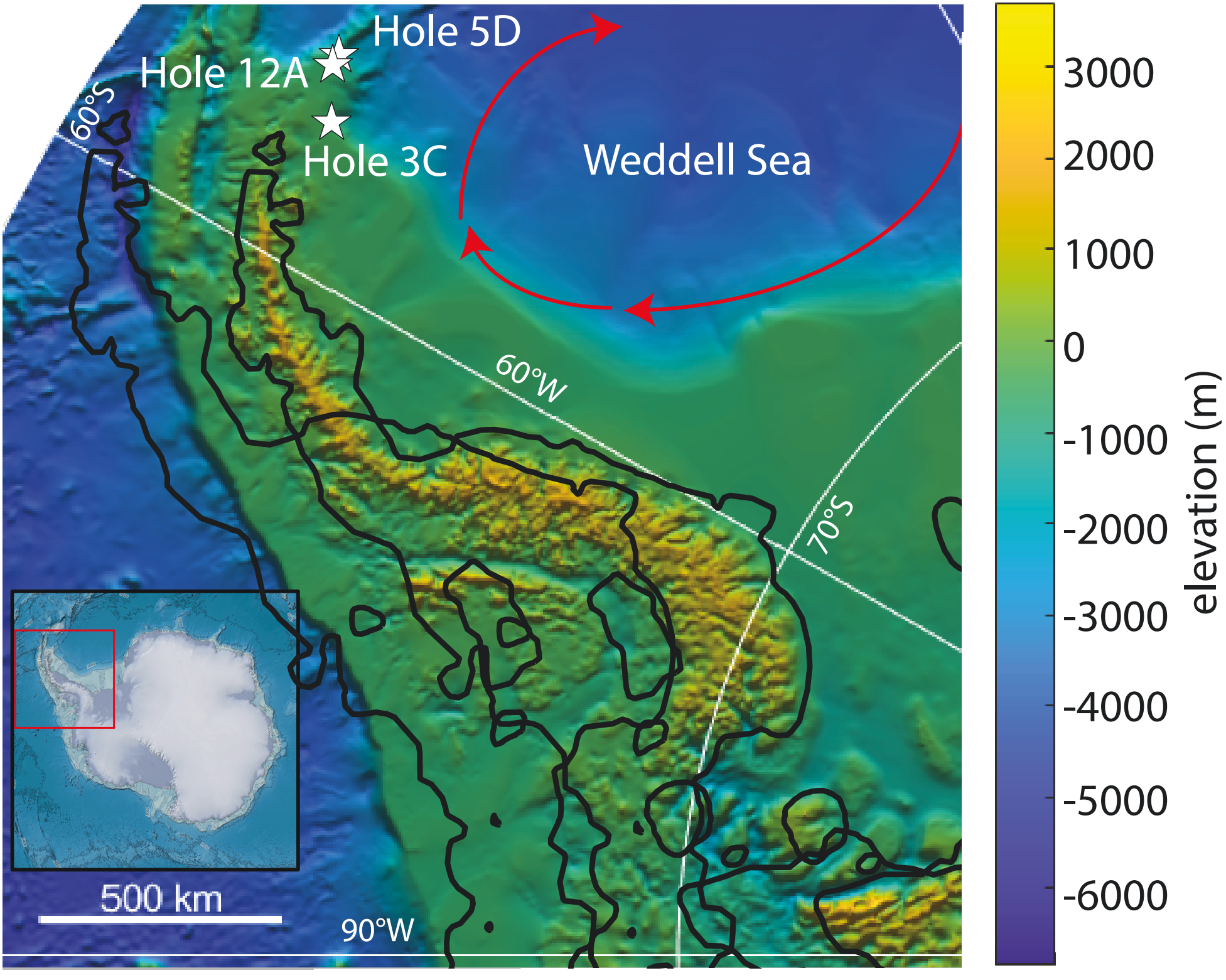
Hole 5D
Hole 12A
Hole 3C
Weddell Sea
60°S
60°W
70°S
90°W
500 km
3000
2000
1000
0
-1000
-2000
-3000
-4000
-5000
-6000
elevation (m)

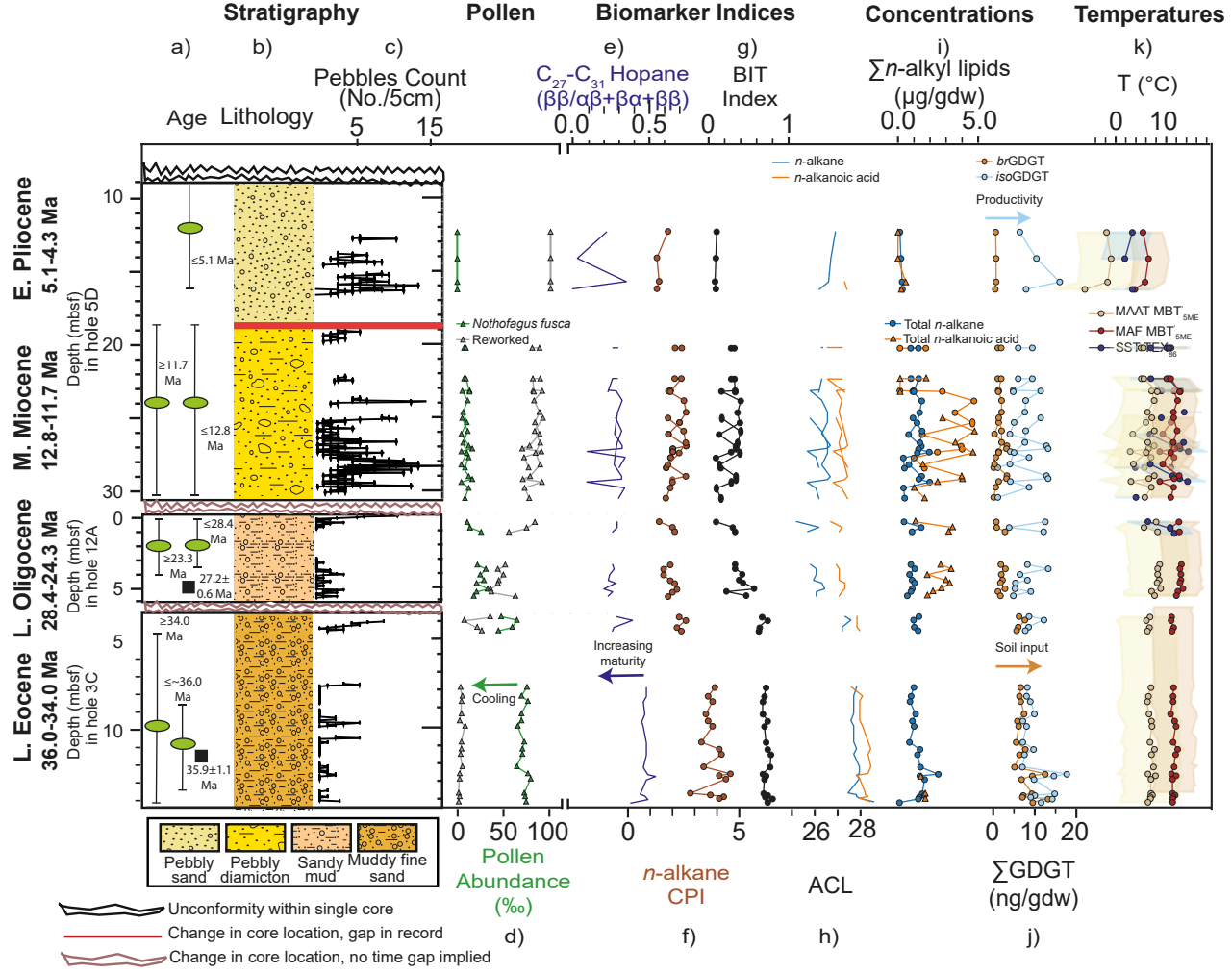
Stratigraphy
Pollen
Biomarker Indices
Concentrations
Temperatures
a)
b)
c)
Age
Lithology
Pebbles Count (No./5cm)
e)
C27-C31 Hopane (ββ/αβ+βα+ββ)
g)
BIT Index
i)
∑n-alkyl lipids (μg/gdw)
k)
T (°C)
E. Pliocene 5.1-4.3 Ma
M. Miocene 12.8-11.7 Ma
L. Oligocene 28.4-24.3 Ma
L. Eocene 36.0-34.0 Ma
Depth (mbsf) in hole 5D
Depth (mbsf) in hole 12A
Depth (mbsf) in hole 3C
≤5.1 Ma
≥11.7 Ma
≤12.8 Ma
≤28.4 Ma
≥23.3 Ma
27.2±0.6 Ma
≥34.0 Ma
≤~36.0 Ma
35.9±1.1 Ma
n-alkane
n-alkanoic acid
brGDGT
isoGDGT
Productivity
Nothofagus fusca
Reworked
Total n-alkane
Total n-alkanoic acid
MAAT MBT5ME
MAF MBT5ME
SST MBT5ME
Increasing maturity
Cooling
Soil input
Pebbly sand
Pebbly diamicton
Sandy mud
Muddy fine sand
Pollen Abundance (‰)
n-alkane CPI
ACL
∑GDGT (ng/gdw)
d)
f)
h)
j)
Unconformity within single core
Change in core location, gap in record
Change in core location, no time gap implied

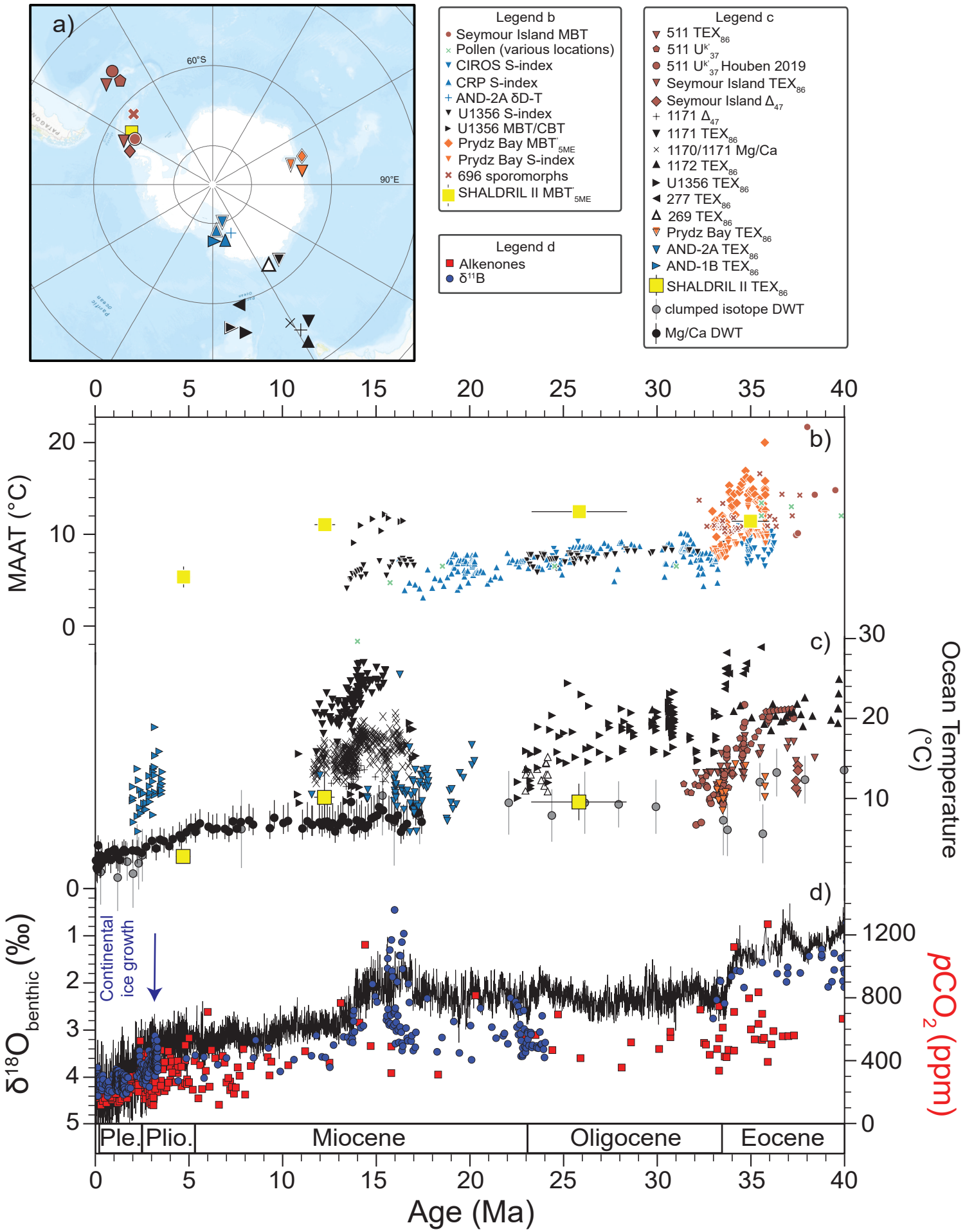
a)
60°S
90°E
Legend b
Seymour Island MBT
Pollen (various locations)
CIROS S-index
CRP S-index
AND-2A δD-T
U1356 S-index
U1356 MBT/CBT
Prydz Bay MBT'5ME
Prydz Bay S-index
696 sporomorphs
SHALDRIL II MBT'5ME
Legend c
511 TEX86
511 UK'37
511 UK'37 Houben 2019
Seymour Island TEX86
Seymour Island Δ47
1171 Δ47
1171 TEX86
1170/1171 Mg/Ca
1172 TEX86
U1356 TEX86
277 TEX86
269 TEX86
Prydz Bay TEX86
AND-2A TEX86
AND-1B TEX86
SHALDRIL II TEX86
clumped isotope DWT
Mg/Ca DWT
Legend d
Alkenones
δ11B
b)
c)
d)
MAAT (°C)
Ocean Temperature (°C)
δ18Obenthic (‰)
pCO2 (ppm)
Continental ice growth
Ple.
Plio.
Miocene
Oligocene
Eocene
Age (Ma)

Paleoceanography and Paleoclimatology

Supporting Information for

Cenozoic Antarctic Peninsula temperatures and glacial erosion signals from a multi-proxy biomarker study

Emily J Tibbett[1], Sophie Warny[2], Jessica E. Tierney[3], Julia S. Wellner[4], Sarah J Feakins[1]

[1]Department of Earth Science, University of Southern California, Los Angeles, CA, USA
[2]Department of Geology and Geophysics, Louisiana State University, Baton Rouge, LA, USA
[3]Department of Geosciences, University of Arizona, Tucson, AZ, USA
[4]Department of Earth and Atmospheric Sciences, University of Houston, Houston, TX, USA

Contents of this file

Introduction

The supporting information associated with the manuscript referenced above includes two supplementary figures. Figure S1 is a map of the modern day Antarctic Peninsula with the paleocoastline from 34 Ma outlined. Figure S2 contains the cluster analysis for the *n*-alkanoic acids, which indicated minimal difference in the abundance of C_{26} and C_{28} dominance between cluster 1 and 2, and overall distributions indicative of penecontemporary (fresh) inputs. Figure S3 contains the cluster analysis for the *n*-alkanes, which includes penecontemporary (cluster 1) and mature components (cluster 2 and 3).

Supplementary Figures

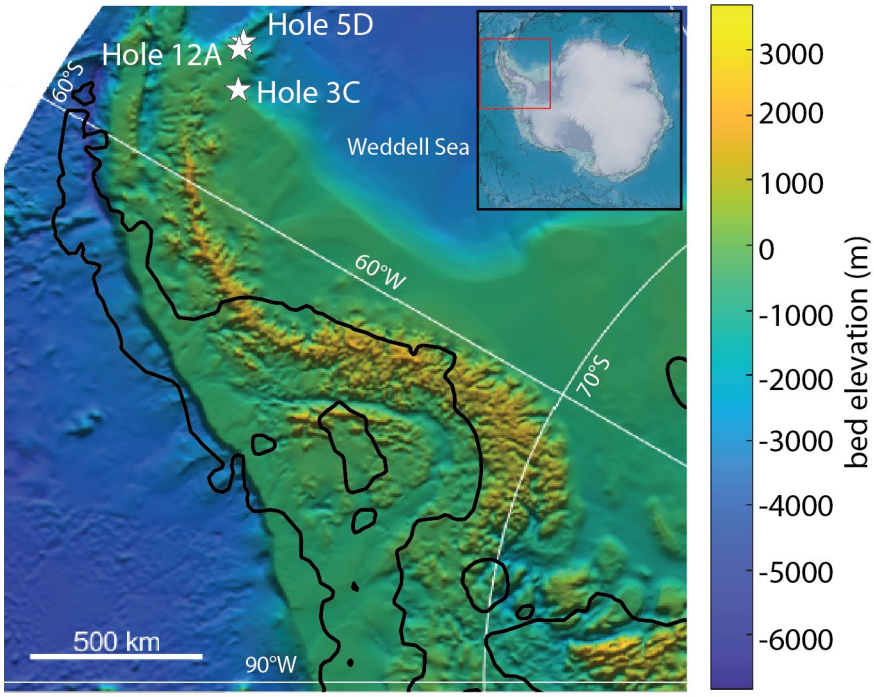

Figure S1. Present day Antarctic bed elevation from bedmap2 (Fretwell et al., 2013) with the Eocene (34 Ma) coastline (Hochmuth et al., 2020) outlined in black. This shows the modest longitudinal rotation of the peninsula since the Eocene.

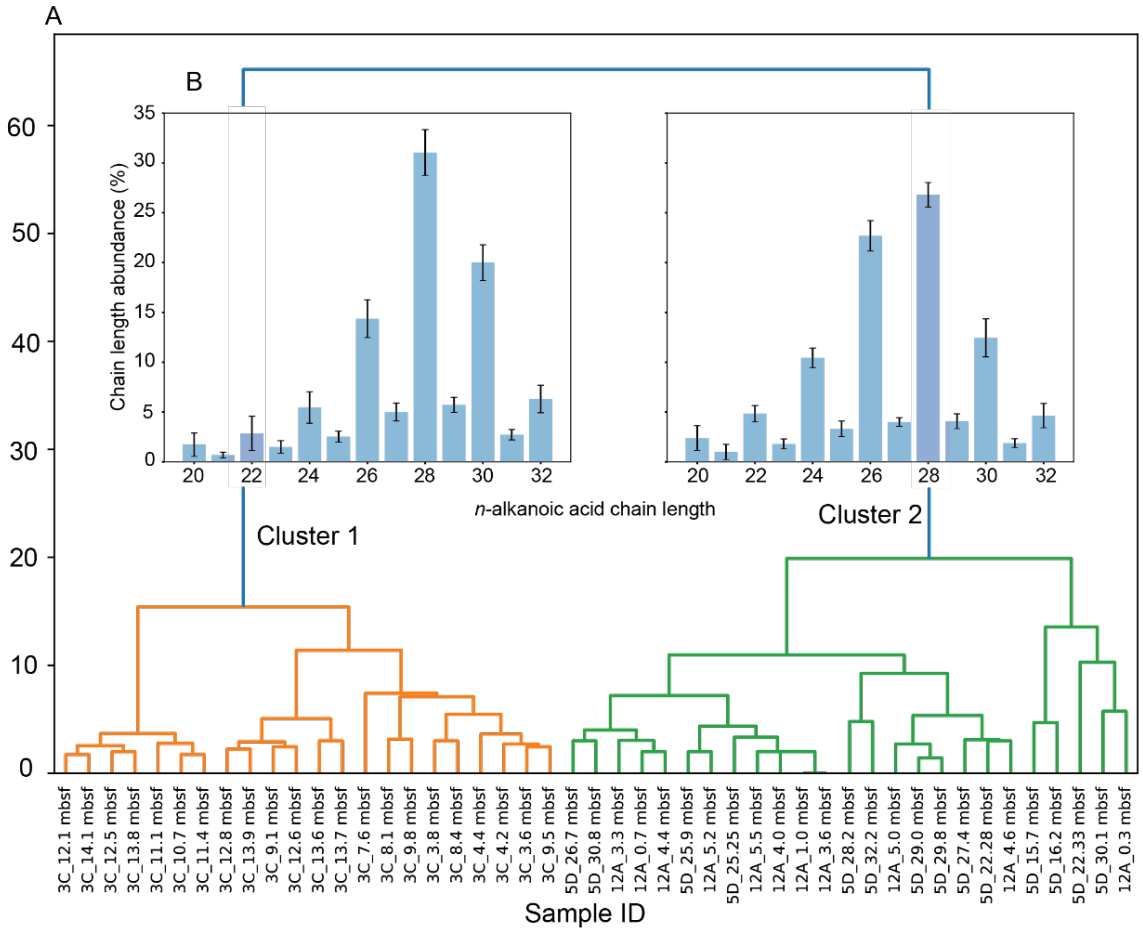

Figure S2. a) Dendrogram of *n*-alkanoic acid chain length distributions with clusters labeled and showing b) molecular abundance distribution, showing mean (bars) and 1 standard deviation (error bars) for each cluster.

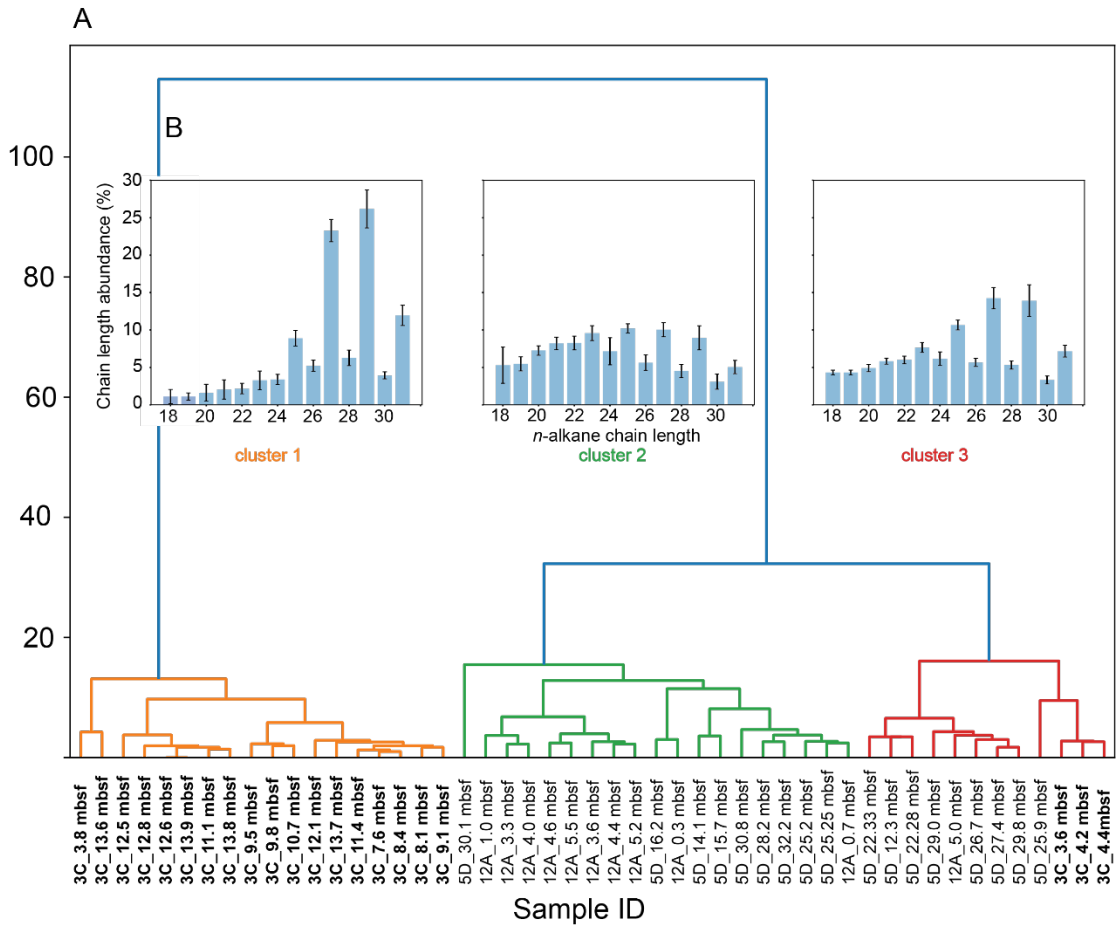

Figure S3. a) Dendrogram of *n*-alkane chain length distributions with clusters labeled and showing b) molecular abundance distribution, showing mean (bars) and 1 standard deviation (error bars) for each cluster. Samples labelled (core_depth) from cores 3C (Eocene), 12A (Oligocene), 5D (middle Miocene and Pliocene). Eocene samples (3C, bold) are mostly in cluster 1 with plant-like distributions of *n*-alkanes, but three samples are in cluster 3 along with samples from 5D, with low CPI components, denoting mature inputs.